NASA
Technical
Paper
3259

March 1993

IN-02
160296
p-30

Conical Euler Analysis and Active Roll Suppression for Unsteady Vortical Flows About Rolling Delta Wings

Elizabeth M. Lee-Rausch
and John T. Batina

(NASA-TP-3259) CONICAL EULER ANALYSIS AND ACTIVE ROLL SUPPRESSION FOR UNSTEADY VORTICAL FLOWS ABOUT ROLLING DELTA WINGS (NASA) 30 p

N93-26134

Unclas

H1/02 0160296

NASA

491809

NASA
Technical
Paper
3259

1993

Conical Euler Analysis and Active Roll Suppression for Unsteady Vortical Flows About Rolling Delta Wings

Elizabeth M. Lee-Rausch
and John T. Batina
Langley Research Center
Hampton, Virginia

NASA
National Aeronautics and
Space Administration
Office of Management
Scientific and Technical
Information Program

ORIGINAL CONTAINS
COLOR ILLUSTRATIONS

Abstract

A conical Euler code was developed to study unsteady vortex-dominated flows about rolling, highly swept delta wings undergoing either forced motions or free-to-roll motions that include active roll suppression. The flow solver of the code involves a multistage, Runge-Kutta time-stepping scheme that uses a cell-centered, finite-volume, spatial discretization of the Euler equations on an unstructured grid of triangles. The code allows for the additional analysis of the free-to-roll case by simultaneously integrating in time the rigid-body equation of motion with the governing flow equations. Results are presented for a delta wing with a 75° swept, sharp leading edge at a free-stream Mach number of 1.2 and at 10°, 20°, and 30° angle of attack α. At the lower angles of attack (10° and 20°), forced-harmonic analyses indicate that the rolling-moment coefficients provide a positive damping, which is verified by free-to-roll calculations. In contrast, at the higher angle of attack (30°), a forced-harmonic analysis indicates that the rolling-moment coefficient provides negative damping at the small roll amplitudes. A free-to-roll calculation for this case produces an initially divergent response, but as the amplitude of motion grows with time, the response transitions to a wing-rock type of limit cycle oscillation, which is characteristic of highly swept delta wings. This limit cycle oscillation may be actively suppressed through the use of a rate-feedback control law and antisymmetrically deflected leading-edge flaps. Descriptions of the conical Euler flow solver and the free-to-roll analysis are included in this report. Results are presented that demonstrate how the systematic analysis of the forced response of the delta wing can be used to predict the stable, neutrally stable, and unstable free response of the delta wing. These results also give insight into the flow physics associated with unsteady vortical flows about delta wings undergoing forced motions and free-to-roll motions, including the active suppression of the wing-rock type phenomenon. The conical Euler methodology developed is directly extendable to three-dimensional calculations.

Introduction

In recent years, the understanding and prediction of the complex flows about high-performance aircraft at high angles of attack have generated much interest within the fluid dynamics community. (See refs. 1 and 2.) These aircraft typically have thin, highly swept lifting surfaces that produce vortical flow over the leeward side of the vehicle at high angles of attack. This vortical flow can have beneficial effects, such as lift augmentation at high angles of attack, on performance. However, it also may have adverse effects, such as structural fatigue due to tail buffet and stability and control problems due to wing rock, wing drop, nose slice, and pitch-up. (See ref. 3.) Consequently, considerable experimental work has been done to understand the basic flow physics of vortical flows about delta wings at high angles of attack. Experimental research efforts directed toward understanding and documenting steady vortical flows are typified by the detailed flow-field measurements about simple-delta, cranked-delta, and canard-delta wing configurations at low speed (ref. 4) and the low-speed tests on a 75° swept delta wing (ref. 5). For supersonic free-stream Mach numbers, vortical flows have been measured by Squire (ref. 6) for an elliptic cone delta wing and by Miller and Wood (ref. 7) for a series of swept sharp-leading-edge delta wings. Experiments to investigate unsteady vortical flows for forced harmonic and free-to-roll motions of an 80° swept delta wing at low speeds have been reported in reference 8. This wing underwent self-induced periodic roll oscillations known as "wing rock" for angles of attack greater than 25°. Levin and Katz (ref. 9) tested 76° swept and 80° swept delta wings and found that only the 80° model exhibited

wing rock at high angles of attack. Further studies have been performed by Jun and Nelson (ref. 10) and Arena and Nelson (ref. 11). These studies show, for example, the time histories of the vortex core position during a cycle of wing rock (ref. 10) and the static and dynamic effects due to vortex breakdown (ref. 11). Also, reference 12 contains experimental water-tunnel results that show wing rock for several delta wing planforms along with detailed flow visualization diagrams. Although much work remains to be done, references 4 to 12 have contributed significantly to the understanding of steady and unsteady vortex-dominated flow fields.

From a computational point of view, considerable effort also has been spent on developing methods for predicting steady and unsteady vortex-dominated flows. (See refs. 13 and 14.) Hoeijmakers (ref. 13) gives a review of computational methods for the determination of steady vortical flow characteristics with an emphasis on classical methods such as discrete vortex, cloud in cell, panel, vortex layer with finite core, leading-edge suction analogy, and vortex lattice. With respect to unsteady methods, a nonlinear mathematical model is presented in reference 15 for calculating wing-rock characteristics based on aerodynamic derivatives that are evaluated using steady-flow aerodynamics. Wing rock was simulated in references 16 to 18 by using an unsteady vortex-lattice method to predict the aerodynamic loads, and the equation of rolling motion was integrated by using a predictor-corrector method. The methods of references 15 to 18 were used to predict, with reasonable accuracy, the low-speed wing-rock characteristics of the delta wings studied in references 8 and 9. Use of the more modern computational fluid dynamics techniques for the prediction of vortex-dominated flows (ref. 14) has focused primarily on steady applications (refs. 19 to 26); there are notable exceptions where applications have been made to rolling delta wings that were undergoing forced harmonic (refs. 27 to 29) and free-to-roll (ref. 30) motions. Kandil and Chuang, for example, calculated flows past rolling delta wings by using the conical Euler equations for sharp-leading-edge wings (ref. 27) and the conical Navier-Stokes equations for rounded-leading-edge wings (ref. 28). In reference 29, results for a rolling delta wing were computed with a conical Euler flow solver on an unstructured grid of triangles. The methods of reference 29 were extended in references 30 to 32 to include a free-to-roll capability, and results are shown for a freely rolling delta wing that exhibited a limit cycle or wing-rock type motion that is characteristic of highly swept delta wings. Subsequent delta-wing calculations obtained by using the conical Euler equations on a structured mesh also exhibited limit cycle oscillations at high angles of attack. (See ref. 33.)

The objective of the current research is to study unsteady, vortex-dominated flow fields by using the conical Euler equations as a first step in investigating the three-dimensional problem. The purpose of this paper is to report on the development of a conical Euler analysis method to study unsteady, vortex-dominated flows about rolling delta wings undergoing either pulsed motion, forced harmonic motion, or free-to-roll motion that includes active roll suppression. Descriptions of the conical Euler flow solver and free-to-roll analysis are included. The flow solver involves a multistage, Runge-Kutta time-stepping scheme and a cell-centered, finite-volume, spatial discretization of the Euler equations on an unstructured grid of triangles. The code was modified to include the simultaneous time integration of the rigid-body equation of motion with the governing flow equations to allow for the additional analysis of the free-to-roll case. The analysis also includes a capability for implementing an active feedback control law with antisymmetrically deflected leading-edge flaps for suppression of the wing-rock motion. Limited experimental and numerical work has been conducted on the use of flaps (refs. 34 and 35) and leading-edge blowing (refs. 36 and 37) for roll control. Results are presented herein for a 75° swept, sharp-leading-edge delta wing at a free-stream Mach number of 1.2 and at 10°, 20°, and 30° angle of attack. These results demonstrate how the systematic analysis of the forced response of the delta wing can be used to predict the stable, unstable, and neutrally stable free response of the delta wing. These results also give insight into the flow physics associated with unsteady vortical flows about delta wings that are undergoing forced motions and free-to-roll motions, including the active suppression of the wing-rock type phenomenon.

Symbols

a_∞	free-stream speed of sound
C_1	$= \frac{M_\infty^2 S c^3 \rho_\infty}{2 I_{xx}}$
C_2	$= \frac{\mu_x c}{a_\infty I_{xx}}$
C_l	rolling-moment coefficient
C_{l_δ}	transfer function of rolling-moment coefficient due to flap deflection
C_{l_ϕ}	transfer function of rolling-moment coefficient due to roll

c	root chord of wing
e	total energy
I_{xx}	mass moment of inertia about longitudinal axis
i	imaginary unit, $\sqrt{-1}$
K_v	control gain
k	reduced frequency of oscillation based on half the root chord, $\frac{\omega c}{2U_\infty}$
l	rolling moment, positive clockwise when viewed from aft
M_∞	free-stream Mach number
p	fluid pressure
p_t	total pressure loss
q_∞	free-stream dynamic pressure
S	planform area
T	transpose operator
t	dimensional time
$\bar{t}$	nondimensional time, $\frac{ta_\infty}{c}$
$\bar{t}_c$	nondimensional time at center of pulse
U, V, W	contravariant velocities in x, y, and z directions
U_∞	free-stream velocity
u, v, w	components of velocity vector in x, y, and z directions
x, y, z	Cartesian coordinates
α	angle of attack
γ	ratio of specific heats
ΔE	energy exchange during harmonic cycle
$\Delta\overline{E}$	normalized energy exchange during harmonic cycle
Δt	dimensionalized global time step
$\Delta\bar{t}$	nondimensional time step
δ	leading-edge flap deflection angle, positive clockwise when viewed from aft
μ_x	structural damping
ρ	density
ρ_∞	free-stream density
ϕ	instantaneous roll angle, positive clockwise when viewed from aft
ϕ_o	harmonic and pulse roll-angle amplitude
ω	frequency, radians per second

Primes with symbols indicate differentiation with respect to nondimensional time.

Governing Equations

The flow is governed by the time-dependent Euler equations, which may be written in conservation-law form as

$$\frac{\partial \mathbf{Q}}{\partial t} + \frac{\partial \mathbf{E}}{\partial x} + \frac{\partial \mathbf{F}}{\partial y} + \frac{\partial \mathbf{G}}{\partial z} = 0 \tag{1}$$

where $\mathbf{Q}$ is the vector of conserved variables defined by

$$\mathbf{Q} = [\rho, \rho u, \rho v, \rho w, e]^T \tag{2}$$

and $\mathbf{E}$, $\mathbf{F}$, and $\mathbf{G}$ are the convective or inviscid fluxes given by

$$\mathbf{E} = \begin{bmatrix} \rho U \\ \rho U u + p \\ \rho U v \\ \rho U w \\ (e+p)\,U + x_t p \end{bmatrix} \tag{3a}$$

$$\mathbf{F} = \begin{bmatrix} \rho V \\ \rho V u \\ \rho V v + p \\ \rho V w \\ (e+p)\,V + y_t p \end{bmatrix} \tag{3b}$$

$$\mathbf{G} = \begin{bmatrix} \rho W \\ \rho W u \\ \rho W v \\ \rho W w + p \\ (e+p)\,W + z_t p \end{bmatrix} \tag{3c}$$

The contravariant velocities U, V, and W are defined by

$$\left.\begin{aligned} U &= u - x_t \\ V &= v - y_t \\ W &= w - z_t \end{aligned}\right\} \tag{4}$$

where x_t, y_t, and z_t are the grid speeds in the x, y, and z directions, respectively. The pressure p is

determined by the equation of state for a perfect gas as follows:

$$p = (\gamma - 1)\left[e - \frac{1}{2}\rho\left(u^2 + v^2 + w^2\right)\right] \tag{5}$$

Equations (1) to (5) have been nondimensionalized by the free-stream density and the free-stream speed of sound.

If interest is restricted to supersonic flow past conical bodies, the conical-flow assumption that is exact for steady inviscid supersonic flow can be made. This assumption reduces the problem from three dimensions to two dimensions, which significantly decreases the computational resources that are required to investigate such flows. For unsteady flows, however, the conical assumption implies instantaneous propagation along radial lines. The following change of variables is then required:

$$\left.\begin{aligned} \xi &= x \\ \eta &= \frac{y}{x} \\ \zeta &= \frac{z}{x} \end{aligned}\right\} \tag{6}$$

The three-dimensional Euler equations then reduce to

$$\frac{\partial \mathbf{Q}}{\partial t} + \frac{\partial}{\partial \eta}(\mathbf{F} - \eta\mathbf{E}) + \frac{\partial}{\partial \zeta}(\mathbf{G} - \zeta\mathbf{E}) + 2\mathbf{E} = 0 \tag{7}$$

Equation (7) may be rewritten in integral form for solution as

$$\frac{\partial}{\partial t}\int_{\Omega}\mathbf{Q}\, d\eta\, d\zeta + \int_{\partial\Omega}[(\mathbf{F} - \eta\mathbf{E})\, d\zeta - (\mathbf{G} - \zeta\mathbf{E})\, d\eta] + \int_{\Omega} 2\mathbf{E}\, d\eta\, d\zeta = 0 \tag{8}$$

where Ω is the integration area and the second integral is a boundary integral that results from application of the divergence theorem.

Solution Algorithm

In this section, an algorithm for the solution of the unsteady conical Euler equations on an unstructured mesh of triangles is described. Conceptually, this spatial discretization reduces to central differencing on a rectangular mesh.

Spatial Discretization

The conical Euler equations in integral form (eq. (8)) are solved numerically by using a finite-volume algorithm developed for analysis with an unstructured grid that is made up of triangles. The algorithm is a cell-centered scheme in which the flow variables are stored at the centroid of each triangle; the control volumes are the triangular elements of the mesh. The boundary integral in equation (8) is formed by the fluxes **E**, **F**, and **G** evaluated at the midpoint of each edge of a given triangular element. The inviscid fluxes at the midpoint at each edge are evaluated with a cell-centered type of approach in which the fluxes of two adjacent elements are averaged across a common edge. For example, along element edge m-k in figure 1, the contribution to the boundary integral in equation (8) for element i is given by

$$(\mathbf{F}_{mk} - \eta_{mk}\mathbf{E}_{mk})(\zeta_m - \zeta_k) - (\mathbf{G}_{mk} - \zeta_{mk}\mathbf{E}_{mk})(\eta_m - \eta_k) \tag{9}$$

where

$$\eta_{mk} = \frac{1}{2}(\eta_m + \eta_k) \tag{10a}$$

$$\zeta_{mk} = \frac{1}{2}(\zeta_m + \zeta_k) \tag{10b}$$

$$\mathbf{E}_{mk} = \frac{1}{2}(\mathbf{E}_i + \mathbf{E}_j) \tag{10c}$$

$$\mathbf{F}_{mk} = \frac{1}{2}(\mathbf{F}_i + \mathbf{F}_j) \tag{10d}$$

$$\mathbf{G}_{mk} = \frac{1}{2}(\mathbf{G}_i + \mathbf{G}_j) \tag{10e}$$

Artificial Dissipation

Artificial dissipation is added explicitly to prevent oscillations near shock waves and to damp high-frequency, uncoupled error modes. Specifically, an adaptive blend of harmonic and biharmonic operators corresponding to second- and fourth-difference dissipation, respectively, is used; this blend is similar to the dissipation described in reference 38. The biharmonic operator provides a background dissipation to damp high-frequency errors, and the harmonic operator prevents oscillations near shock waves. The harmonic operator is multiplied by a pressure switch that is first-order accurate near shocks and second-order accurate in smooth regions of the flow. The biharmonic operator is third-order accurate and is adaptively turned off to prevent overshoots in regions of shock waves. The harmonic-difference operator stencil for element i with surrounding neighbors 1, 2, and 3 is shown in figure 2. For elements adjacent to a boundary, image or "ghost" cells are used to complete the stencil shown in figure 2. The values of the conserved variables associated with the image cells are determined by the type of boundary that the

shared edge represents. If the boundary is a solid wall, then the normal and tangential velocities are set in the image cell so that a free-to-slip condition is imposed on the boundary edge. Specifically, the normal velocity in the image cell is set opposite to that of the adjacent interior cell; tangential velocity is simply mirrored, so that when the velocities are averaged across the boundary edge, a flow tangency condition is enforced. The pressure and density are reflected into the image cells such that a zero normal derivative is imposed on the boundary edge. If a cell is adjacent to a far-field boundary, then the conserved variables in the adjacent image cell are set to free-stream conditions. This boundary condition requires that the bow shock be captured within the interior of the computational domain. The biharmonic operator for an element is computed with second-difference terms from the harmonic operators. Along the boundaries, the second-difference term in the image cell is simply set equal to its value in the parent cell, so that no additional ghost cells are required at the boundaries.

Boundary Conditions

The boundary conditions are enforced by specifying the fluxes along boundary edges for use in the evaluation of the boundary integral in equation (9). For those edges along the far-field boundary, free-stream conditions are applied with the assumption that the bow shock is captured. To impose a no-flow-through boundary along the surface of the body, the boundary integral in equation (8) is first rewritten in terms of the flux velocity defined by

$$(V - \eta U)\,\Delta\zeta - (W - \zeta U)\,\Delta\eta \tag{11}$$

For edges along the solid boundary, this flux velocity, which is proportional to the velocity normal to the edge, is then set equal to zero. The pressure terms along the solid boundary edge are evaluated in the boundary integral with the cell-center values.

Time Integration

The conical Euler equations are integrated in time by assuming that the conserved variables represented by $\mathbf{Q}$ are constant within a control volume which yields

$$\frac{d}{dt}\left(A_i \mathbf{Q}_i\right) + C\left(\mathbf{Q}_i\right) - D\left(\mathbf{Q}_i\right) = 0 \tag{12}$$

where C and D are the convective and dissipative operators, respectively, and A_i is the area surrounding element i. These equations are integrated in time by using an explicit four-stage, Runge-Kutta, time-stepping scheme given by

$$\left.\begin{aligned}
\mathbf{Q}^{(0)} &= \mathbf{Q}^n \\
\mathbf{Q}^{(1)} &= \frac{A^n}{A^{n+1}}\mathbf{Q}^{(0)} - \frac{1}{4}\frac{\Delta t}{A^{n+1}}\left[C\left(\mathbf{Q}^{(0)}\right) - D\left(\mathbf{Q}^{(0)}\right)\right] \\
\mathbf{Q}^{(2)} &= \frac{A^n}{A^{n+1}}\mathbf{Q}^{(0)} - \frac{1}{3}\frac{\Delta t}{A^{n+1}}\left[C\left(\mathbf{Q}^{(1)}\right) - D\left(\mathbf{Q}^{(0)}\right)\right] \\
\mathbf{Q}^{(3)} &= \frac{A^n}{A^{n+1}}\mathbf{Q}^{(0)} - \frac{1}{2}\frac{\Delta t}{A^{n+1}}\left[C\left(\mathbf{Q}^{(2)}\right) - D\left(\mathbf{Q}^{(0)}\right)\right] \\
\mathbf{Q}^{(4)} &= \frac{A^n}{A^{n+1}}\mathbf{Q}^{(0)} - \frac{\Delta t}{A^{n+1}}\left[C\left(\mathbf{Q}^{(3)}\right) - D\left(\mathbf{Q}^{(0)}\right)\right] \\
\mathbf{Q}^{n+1} &= \mathbf{Q}^{(4)}
\end{aligned}\right\} \tag{13}$$

where Δt is the global time step and the superscript n represents the value at the time level n. In this scheme, the convective operator is evaluated at each stage; for computational efficiency, the dissipative operator is evaluated only at the first stage. The Runge-Kutta scheme represented by equations (13) is second-order accurate in time and includes the necessary terms to account for changes in cell areas as the result of a moving or deforming mesh.

Implicit Residual Smoothing

The explicit time-integration scheme described in the preceding section has a step size that is limited by the Courant-Friedrichs-Lewy (CFL) condition corresponding to a CFL number of $2\sqrt{2}$. To accelerate convergence to the steady state, the CFL number may be increased by averaging the residual $\mathbf{R}_i$ with values at neighboring elements. This residual averaging is accomplished by replacing $\mathbf{R}_i$ with the smoothed residual $\overline{\mathbf{R}}_i$ given by

$$\overline{\mathbf{R}}_i - \epsilon\nabla^2\overline{\mathbf{R}}_i = \mathbf{R}_i \tag{14}$$

where ϵ is a constant that controls the amount of smoothing and ∇^2 is an undivided Laplacian operator. These implicit equations are solved approximately by using several Jacobi iterations similar to those in references 38 and 39.

For steady-state calculations, convergence is further accelerated by using enthalpy damping (ref. 40) and local time stepping. The local time stepping uses the maximum allowable step size at each grid point as determined by a local stability analysis. For unsteady applications, however, a global time step must be used because of the time-accuracy requirement. By using a time-accurate version of equation (14) similar to that of reference 41, the maximum allowable global time step may be increased to a value

that is larger than that dictated by the CFL condition. In this procedure, the constant ϵ is replaced by a parameter defined by

$$\epsilon = \max\left[\frac{1}{4}\left(\frac{\Delta t^2}{\Delta t^2_{\mathrm{CFL}}} - 1\right), 0.0\right] \tag{15}$$

which varies from grid point to grid point. In equation (15), Δt is the time step taken and Δt_{CFL} is the locally allowable time step for the four-stage Runge-Kutta time-stepping scheme.

Deforming-Mesh Algorithm

The deforming-mesh algorithm, as developed in reference 42, models the triangular mesh as a spring network in which each edge of a triangle represents a spring with stiffness inversely proportional to the square of its length. In this method, the grid points along the outer boundary are held fixed, and the grid points along the wing (inner boundary) are specified. The locations of the interior points are then determined by solving the static equilibrium equations, which result from a summation of forces at each node in the η and ζ directions. The solution of the equilibrium equations is carried out by using a predictor-corrector method that first predicts the new locations of the interior points by extrapolation from the previous time levels and then corrects these locations by using several Jacobi iterations of the static equilibrium equations. The predictor-corrector procedure is relatively efficient, since it requires only a few Jacobi iterations to adequately move the mesh.

Pulse Transfer-Function Analysis

Generally, unsteady load coefficients can be obtained by calculating several cycles of a forced-harmonic oscillation and using the last cycle of oscillation to determine the load. This process requires one flow-field calculation for each value of reduced frequency of interest. In contrast, the unsteady load coefficients may be determined for a wide range of reduced frequency in a single flow-field calculation by using the pulse transfer-function analysis. The pulse transfer-function analysis has been used previously to determine the generalized aerodynamic forces (GAF), which are used in aeroelastic analyses. (See refs. 43 and 44.) In the pulse analysis, the unsteady load coefficient is computed indirectly from the response of the flow field as a result of motion that is represented by a smoothly varying, exponentially shaped pulse. Results computed by using the pulse analysis for a pitching flat-plate airfoil were in good agreement with parallel linear-theory calculations. (See ref. 44.) Reference 44 also shows that the GAF airfoils at transonic speeds that were computed from a pulse analysis were in good agreement with the GAF values that were computed by using the harmonic method, which tends to verify that the analysis is valid for predicting the small perturbation response about a nonlinear flow field. These calculations verify the accuracy of the pulse analysis. Therefore, because of the computational efficiency of the pulse transfer-function analysis, the capability was implemented within the conical Euler code to calculate the rolling-moment coefficient due to roll C_{l_ϕ} of a delta wing. The pulse in roll angle is expressed as

$$\phi\left(\bar{t}\right) = \phi_o \exp\left[-M_\infty^2\left(\bar{t} - \bar{t}_c\right)^2\right] \tag{16}$$

where ϕ_o is the pulse amplitude, M_∞ is the free-stream Mach number, which determines the width of the pulse, and $\bar{t}_c$ is the nondimensional time at the center of the pulse. While a small pulse in roll angle is prescribed for the delta wing, the aerodynamic transient is calculated. By using a transfer-function analysis, this aerodynamic transient is then used to obtain the rolling-moment coefficient in the frequency domain. In this case, a fast Fourier transform (FFT) of the rolling-moment coefficient is divided by an FFT of the pulsed rolling motion to obtain the value of C_{l_ϕ}. The transform assumes that the system is locally linear. Additional work not reported in this study has shown this assumption to be valid for the pulse amplitude of 1° used in the present study.

Forced-Harmonic Analysis

Because the pulse analysis is limited to small perturbations, the large-perturbation aerodynamic response characteristics of the rolling delta wing are determined using a forced-harmonic analysis. The forced-harmonic rolling motion can be expressed as

$$\phi\left(\bar{t}\right) = \phi_o \sin\left(k\bar{t}\right) \tag{17}$$

where ϕ_o is now the roll amplitude, k is the reduced frequency of oscillation (based on half the wing root chord), and $\bar{t}$ is the nondimensional time. Since the linear techniques are no longer applicable, the concept of energy transferred to the system can be used in this analysis to determine the stability characteristics. A similar technique was applied experimentally in reference 8 for the analysis of wing-rock aerodynamics. During 1 cycle of harmonic motion, the total aerodynamic energy added to the system is

$$\Delta E = \oint C_l \, d\phi \tag{18}$$

where ΔE is a nondimensional energy and C_l is the rolling-moment coefficient. If $\Delta E > 0$, then the aerodynamic forces are adding energy to the wing, which would have a destabilizing effect on the free-to-roll response. If $\Delta E < 0$, then the aerodynamic forces are extracting energy from the wing, which would have a stabilizing effect on the free-to-roll response. Equation (18) indicates that for the rolling-moment coefficient versus roll-angle response, which traces a clockwise loop during 1 cycle of motion, the energy exchange is positive during the cycle. Similarly, for a counterclockwise loop, the energy exchange is negative. If multiple loops are formed, then ΔE is a total of the individual loops.

Free-to-Roll Analysis

Roll Equation of Motion

The equation of motion for a rolling delta wing can be expressed as

$$I_{xx}\ddot{\phi} = l - \mu_x\dot{\phi} \tag{19}$$

where ϕ is the roll angle which is positive clockwise when viewed from aft, I_{xx} is the mass moment of inertia about the longitudinal axis, l is the aerodynamic rolling moment, also positive clockwise, and μ_x is a structural damping term. (Dots over symbols indicate differentiation with respect to time.) To nondimensionalize equation (19), the angular rates are multiplied by the root chord of the delta wing c and divided by the free-stream speed of sound a_∞. The rolling-moment coefficient is defined as

$$C_l = \frac{l}{q_\infty S c} \tag{20}$$

where q_∞ is the free-stream dynamic pressure and S is the planform area. The nondimensional rolling equation of motion can then be written as

$$\phi'' = C_1 C_l - C_2\phi' \tag{21}$$

where

$$C_1 = \frac{M_\infty^2 S c^3 \rho_\infty}{2 I_{xx}} \tag{22a}$$

$$C_2 = \frac{\mu_x c}{a_\infty I_{xx}} \tag{22b}$$

The structural damping term is added to simulate the damping that might be provided by a sting-balance bearing mount. This type of bearing mount was used in the low-speed wind-tunnel investigations of wing rock reported in references 8 to 11.

Time-Marching Solution

The solution procedure for the time integration of equation (21) is based on a finite-difference representation of the time derivatives. The time derivatives are expressed in terms of second-order-accurate finite-difference approximations. After substituting these expressions into equation (21), the roll angle at time level $n+1$ can be expressed in terms of the roll angle at previous time levels as

$$\phi^{n+1} = \frac{C_1 C_l^{n+1}\Delta\bar{t}^2 + \left(5 + 2C_2\Delta\bar{t}\right)\phi^n}{\frac{3}{2}C_2\Delta\bar{t} + 2} + \frac{\left(-4 - \frac{1}{2}C_2\Delta\bar{t}\right)\phi^{n-1} + \phi^{n-2}}{\frac{3}{2}C_2\Delta\bar{t} + 2} \tag{23}$$

The rolling moment C_l^{n+1} at time level $n+1$ is estimated from a linear extrapolation of C_l at the previous two time levels. This predicted value of C_l is used to determine the roll angle ϕ^{n+1} at time level $n+1$. The flow field about the wing at this roll angle is then calculated, and the actual value of the rolling-moment coefficient is determined. The rolling-moment coefficient is then updated for use in the next time step. Because of the explicit time marching of the Euler code used in this study, the time steps required for numerical stability were small—approximately 6500 time steps per cycle of motion. Thus, it was not necessary to iterate between the roll angle calculation and the flow-field calculation at each time step. For a free-to-roll calculation, steady-state initial conditions are specified for ϕ^{-1}, ϕ^0, C_l^{-1}, and C_l^0. At $\bar{t} = 0$, an angular velocity perturbation is applied to the wing.

Active Roll Suppression

Active roll suppression is achieved through the addition of an active rate-feedback control law to the time-marching solution procedure. A simple control law was chosen of the form

$$\delta = K_v\phi' \tag{24}$$

where K_v is the control gain and the values of δ are the left and right leading-edge flap deflection angles measured positive clockwise from the flap hinge lines. The control law is applied to the left and right flaps simultaneously, which results in an antisymmetric configuration. The time-marching solution procedure is the same as that described in the preceding section. However, after the roll angle at time level $n+1$ is determined from equation (23), the flap deflection angle is determined from equation (24)

by using a second-order-accurate finite-difference expression for the angular velocity ϕ'. The deforming mesh algorithm is then applied, in addition to the rigid rotation, to move the mesh to its new position. As before, the flow field is calculated about the wing at its new position, and the rolling-moment coefficient is determined and updated for use in the next time step. The same initial conditions described in the preceding section are applied to begin the calculation.

Results and Discussion

Calculations were performed for a 75° swept delta wing at a free-stream Mach number of 1.2 and at $\alpha = 10°$, 20°, and 30°. The wing has thickness and sharp leading edges as indicated in the partial view of the grid shown in figure 3. The thickness-to-span ratio at this cross section is 0.025, and the lower-edge bevel angle is 10°. The grid, which was generated by using an advancing front method (ref. 45), has a total of 4226 nodes and 8299 elements. The grid was designed to be fine on the leeward side of the wing, where the dominant flow features are expected to occur. As discussed previously, the mesh is rotated as a rigid body for unsteady applications to conform to the instantaneous position of the main part of the wing. The mesh is deformed locally near the leading edges to conform to the instantaneous position of the flaps. As examples of mesh movement, partial views of the left leading-edge flap at a positive ($\delta = 10°$) and a negative ($\delta = -10°$) flap deflection angle are shown in figures 4(a) and 4(b), respectively, with the wing rotated through 10° of motion. The hinge point of the flap coincides with the inboard bevel edge on the lower surface; the flap length is therefore approximately 28 percent of the semispan. As shown in the figure, the mesh moves smoothly as the wing rolls and as the flaps are deflected.

Steady and unsteady results, including the pulse, forced-harmonic, and free-to-roll calculations, are presented for $\alpha = 10°$, 20°, and 30°. The rate-feedback control law is applied to the $\alpha = 30°$ case, since it is the only free-to-roll case to exhibit a wing-rock behavior.

Steady-State Results

Steady-state results were obtained to determine the basic character of the vortical flows and to provide starting solutions for the unsteady cases. A comparison of total pressure loss contours from these solutions (fig. 5) illustrates the effects of angle of attack. For the $\alpha = 10°$ case (fig. 5(a)), the contours indicate that the flow separates from each of the leading edges of the wing, which produces two small, widely spaced circular vortices. At $\alpha = 20°$ (fig. 5(b)), the contours indicate that the vortices are now larger than for the $\alpha = 10°$ case. The flow accelerating beneath the vortices at this increased angle of attack also produces two vertically oriented crossflow shock waves on the outboard portions of the wing. For the $\alpha = 30°$ case (fig. 5(c)), the contours indicate that the flow separating from the leading edges produces two large, more closely spaced vortices. Also, as the flow accelerates beneath the vortices (fig. 5(c)), vertically oriented crossflow shock waves are formed on the outboard portions of the wing. Weaker shock waves are formed on the top of each vortex. These vertically oriented shocks are located above the core of the vortex. A weaker horizontal shock wave is also present between the vortices.

Pulse Transfer-Function Results

The pulse transfer-function analysis was performed to determine the small amplitude stability and response characteristics of the wing. A stability analysis was derived by first recalling the nondimensional rolling equation of motion given by

$$\phi'' = C_1 C_l - C_2 \phi' \tag{21}$$

For simplicity, the structural damping term C_2 is set equal to zero, which results in

$$\phi'' = C_1 C_l \tag{25}$$

Assuming that the rolling-moment coefficient can be written as the product of the rolling-moment-coefficient transfer function C_{l_ϕ} and the roll angle ϕ, then

$$C_l = C_{l_\phi} \phi \tag{26}$$

Then, for simple harmonic motion,

$$C_l = [\mathrm{Re}(C_{l_\phi}) + i\mathrm{Im}(C_{l_\phi})]\phi \tag{27}$$

where $\mathrm{Re}(C_{l_\phi})$ and $\mathrm{Im}(C_{l_\phi})$ represent the real and imaginary parts of the first harmonic component of C_{l_ϕ}. In this case, the real part of the rolling-moment-coefficient transfer function represents an aerodynamic stiffness, and the imaginary part represents an aerodynamic damping. Therefore, for this simple one-degree-of-freedom case, the sign of $\mathrm{Im}(C_{l_\phi})$ determines the stability in roll of the wing for small perturbations. In other words, a negative value of $\mathrm{Im}(C_{l_\phi})$ indicates a positive aerodynamic damping, which would cause a free-to-roll wing to be stable; a positive $\mathrm{Im}(C_{l_\phi})$ indicates a negative aerodynamic damping, which would cause a free-to-roll wing to be unstable.

The pulse transfer-function analysis is used to determine the force-coefficient transfer function, and therefore the stability of the wing, for a wide range of reduced frequency k. The nondimensional time step used in these analyses was $\Delta\bar{t} = 0.004$, which results in a frequency resolution of $\Delta k = 0.1$. A comparison of results from the pulse transfer-function analysis (fig. 6) indicates the effects of angle of attack. A maximum pulse amplitude of 1° was used at each angle of attack. However, at $\alpha = 20°$, an additional pulse amplitude of $-1°$ was also considered for reasons explained below. At $\alpha = 10°$ (fig. 6(a)), $\mathrm{Im}(C_{l_\phi})$ is negative for all values of reduced frequency, which is indicative of stability in roll for small perturbations. At $\alpha = 20°$ (fig. 6(b)), $\mathrm{Im}(C_{l_\phi})$ is also negative over all values of reduced frequency for both pulse angles. However, the absolute value of $\mathrm{Im}(C_{l_\phi})$ for each value of k is smaller for $\alpha = 20°$ results than for $\alpha = 10°$ results; thus, the aerodynamic damping should be lower at $\alpha = 20°$. In contrast, at $\alpha = 30°$ (fig. 6(c)), the imaginary part is positive for $k \leq 0.5$, which is indicative of instability in roll. Also, the $\mathrm{Re}(C_{l_\phi})$ is negative for $\alpha = 30°$ in this range of reduced frequency, which corresponds to a positive aerodynamic stiffness. The roll response will therefore oscillate (with increasing amplitude) rather than give rise to a static instability known as wing drop.

The accuracy of the pulse analysis is verified by harmonic analyses performed at five values of reduced frequency: $k = 0.0$, 0.25, 0.50, 0.75, and 1.0. In these analyses, the wing was oscillated harmonically in roll with an amplitude of 1° for three cycles of motion; the rolling-moment coefficient was determined from the last cycle. The nondimensional time step used in all cases was 0.00262, which corresponds to 2600 steps per cycle for the $k = 0.25$ cases and 650 steps per cycle for the $k = 1.0$ cases. The results of the harmonic analyses are compared with the rolling-moment-coefficient transfer functions shown in figure 6. The agreement between pulse and harmonic analyses is very good for $\alpha = 10°$ and 30°. For $\alpha = 20°$, the harmonic results lie between the pulse results for $\phi_o = 1°$ and $\phi_o = -1°$. Because of the initial symmetry of the steady-state configuration, the pulse results should be independent of the sign of the pulse amplitude. However, flow-field asymmetries associated with the asymmetric mesh cause some bias in the pulse-analysis results at this angle of attack that are not present in the harmonic analyses, because the harmonic analyses involve oscillations between $\phi = \pm 1°$. This symmetric motion effectively compensates for the flow-field asymmetries.

Forced-Harmonic Results

Because the pulse transfer-function analysis is limited to small perturbations, the large-perturbation aerodynamic characteristics of the delta wing were investigated with forced-harmonic oscillations. Motions at a reduced frequency of $k = 0.25$ were chosen for this analysis. This value lies at the midpoint of the range of reduced frequency that is identified by the pulse analysis as being an unstable condition for the free-to-roll wing at $\alpha = 30°$. Three amplitudes of motion—$\phi_o = 5°$, 15°, and 35°—were considered at $\alpha = 10°$, 20°, and 30°. The nondimensional time step used for all cases was 0.00262, which corresponds to 4000 steps per cycle of harmonic motion. A comparison of rolling-moment coefficient versus roll angle for each of these cases is shown in figure 7 to illustrate the effects of roll amplitude and angle of attack. For $\alpha = 10°$ (fig. 7(a)), the results indicate a counterclockwise loop for each roll amplitude, which would produce a convergent (stable) response if the wing were free to roll. This prediction of a stable response at the smallest roll amplitude is consistent with the pulse transfer-function results in figure 6(a). Also, as the roll amplitude is increased from 5° to 15°, the maximum rolling-moment coefficient increases linearly. (Note the change in scaling of the vertical and horizontal axes.) However, as the roll amplitude is further increased to 35°, some nonlinear aerodynamic characteristics are exhibited in the "pinching" of the loop at the extreme roll angles; however, the free-to-roll response is still predicted to be stable. Similarly, for $\alpha = 20°$ (fig. 7(b)), the results show a counterclockwise loop ($\Delta E < 0$) for each roll amplitude, which also would produce a stable response if the wing were free to roll. This prediction of a stable response at the smallest roll amplitude, which would be more lightly damped than for $\alpha = 10°$, is also consistent with the pulse transfer-function results of figure 6(b). For $\alpha = 30°$ (fig. 7(c)), the results indicate clockwise loops for the 5° and 15° roll amplitudes, which would produce a divergent (unstable) response if the wing were free to roll. This prediction of an unstable, free-to-roll response at the smaller roll amplitudes is consistent with the pulse transfer-function results of figure 6(c). For $\phi_o = 35°$, counterclockwise loops have formed at the extreme roll angles which, consequently, would have a stabilizing effect on the free-to-roll response. The formation of these stabilizing loops was not, of course, predicted by the pulse analysis. In contrast to the $\alpha = 10°$ and 20° cases, the nonlinear aerodynamic effects at the larger roll amplitudes for $\alpha = 30°$ result in a change in the stability characteristics of the wing.

The total aerodynamic energy exchange during a cycle of motion, as described in equation (18), was calculated for each roll amplitude. These nondimensional energy values were then normalized by a factor of $\phi_o^2 \Delta E_{30}$, where ϕ_o is the roll amplitude during the cycle (in degrees) and ΔE_{30} is the energy exchange value for $\alpha = 30°$ and $\phi_o = 1°$. The normalized energy exchange during the cycle can thus be expressed as

$$\Delta \overline{E} = \frac{\Delta E}{\phi_o^2 \Delta E_{30}} \tag{28}$$

Plots of $\Delta \overline{E}$ versus ϕ_o at each angle of attack are shown in figure 8. Additional results for the roll amplitudes of 1°, 30°, and 45° are included in figure 8. If the aerodynamic effects were linear over the range of roll amplitudes, then the curve of $\Delta \overline{E}$ versus ϕ_o for $\alpha = 30°$ should be a horizontal line at $\Delta \overline{E} = 1$. Similarly, the curves for $\alpha = 10°$ and 20° should be horizontal lines at their respective normalized energy exchange values for $\phi_o = 1°$ if the system was linear. For $\alpha = 10°$ and 20°, the near-horizontal lines shown in figure 8 indicate that the aerodynamic effects are nearly linear with respect to roll amplitude. For $\alpha = 30°$, nonlinear effects are indicated in figure 8 at the larger roll amplitudes, which would result in a change in the stability characteristics of the free-to-roll wing. A neutrally stable condition ($\Delta E = 0$) or limit cycle oscillation is predicted at approximately $\phi_o = 36°$ for this reduced frequency.

The unsteady vortex dynamics during a harmonic cycle can be illustrated by the changes in the crossflow contours during the cycle. Crossflow total-pressure-loss contours from the $\alpha = 30°$ forced-harmonic cases at $\phi_o = 5°$ and 35° are shown in figure 9. The instantaneous crossflow contours are shown at four points in time that correspond to the 0° (1), 90° (2), 180° (3), and 270° (4) cycle positions. For $\phi_o = 5°$ (fig. 9(a)), the contours show only a slight variation in the vortex strength and location during the cycle. However, for $\phi_o = 35°$ (fig. 9(b)), the contours indicate that the vortex strength and location change significantly during the cycle. Figure 9(b) shows that as the left leading edge moves through zero roll angle (position 1) and continues to the maximum position (position 2), the left vortex weakens and lifts off the wing, while the right vortex strengthens and moves inboard. Similarly, as the right leading edge moves through zero roll angle (position 3) to the maximum position (position 4), the right vortex weakens and lifts off the wing, while the left vortex strengthens, reattaches, and moves inboard. This vortex lift-off and reattachment is believed to be the source of the nonlinear variation of the rolling-moment coefficient shown in figures 7 and 8.

Free-to-Roll Results

The free-to-roll results were obtained for the flow conditions and structural and inertial parameter values listed in table 1. The structural and inertial properties used in these calculations are loosely based on the characteristics of the models used in the experimental study of wing rock in reference 9. The initial nondimensional angular velocity imposed on the wing was 0.003, and the nondimensional time step was 0.004. The resulting roll-angle response for the $\alpha = 10°$ case (fig. 10(a)) indicates that, after the initial perturbation, the oscillatory response converges to its initial steady-state value. This stable free-to-roll response is consistent with the pulse and forced-harmonic results presented in figures 6(a) and 7(a). Similarly, the resulting roll-angle response for $\alpha = 20°$ (fig. 10(b)) also shows a stable, converging response that is consistent with the pulse and forced-harmonic results of figures 6(b) and 7(b). Also, as predicted by the pulse and harmonic analyses, the response at $\alpha = 20°$ is more lightly damped than the response at $\alpha = 10°$. The roll-angle response for $\alpha = 30°$ (fig. 10(c)) indicates that the oscillatory response initially diverges for small values of roll angle, which is consistent with the small amplitude pulse and harmonic results of figures 6(c) and 7(c). As the roll angle increases to around 35°, the rate of divergence decreases because of the stabilizing aerodynamics (counterclockwise loops in the rolling-moment coefficient at the extreme roll angles) shown in figure 7(c). Finally, the response reaches a maximum amplitude of motion at approximately $\phi = 38°$; this response corresponds to a limit cycle oscillation. The reduced frequency of the limit cycle is 0.103.

Table 1. Summary of Structural Parameter Values and Flow Conditions for Free-to-Roll Calculation

c, m	0.282
I_{xx}, kg-m^2	0.1776×10^{-3}
μ_x, kg-m^2/sec	0
ρ_∞, kg/m^3	0.526
a_∞, m/sec	312

In the low-speed experimental investigation of wing rock conducted by Arena and Nelson (ref. 11), the wing-rock time history of an 80° swept delta wing at 30° angle of attack exhibited a symmetric growth of the maximum roll angle which, at the larger roll amplitudes, transitioned to a limit cycle

oscillation at $k = 0.125$. During the wing-rock motion, no vortex burst was observed above the configuration. For the high-speed calculations performed in this study, the wing-rock time history exhibited a similar symmetric growth and transition. However, the structured-grid, conical Euler calculation from reference 33 for an 80° swept delta wing at a free-stream Mach number of 1.2 and 35° angle of attack indicated an antisymmetric growth of the maximum roll amplitude that transitioned to a limit cycle oscillation about a mean roll angle of −5°.

Similar to the forced-harmonic results shown in figure 9, the unsteady vortex dynamics during the wing-rock cycle are illustrated in figure 11 by the changes in the crossflow total-pressure-loss contours during the cycle. The instantaneous crossflow contours are shown at four points in time during the wing-rock cycle, these points correspond to the 0° (1), 90° (2), 180° (3), and 270° (4) cycle positions. Figure 11 shows that, similar to the results shown in figure 9(b), as the left leading edge moves through zero roll angle (position 1) and continues to the maximum position (position 2), the left vortex weakens and lifts off the wing and the right vortex strengthens and moves inboard. As the right leading edge moves up to its maximum position (position 4), the right vortex weakens and lifts off the wing and the left vortex strengthens, reattaches, and moves inboard. The similarities between the results of figure 9(b) and figure 11 lead to the conjecture that the vortex lift-off and reattachment are the sources of the change in aerodynamic damping that stabilizes the wing response; thus, a limit cycle oscillation is produced. However, the details of the fluid mechanisms that produce the wing rock are still under investigation.

It is important to address two of the major limitations of the conical Euler equations. The first of these is that the conical Euler equations cannot predict the formation of secondary vortices. However, it is shown in reference 24 that for steady flow, the Euler equations accurately model the primary vortex for a sharp-edge delta wing. The second limitation of the conical Euler equations is that these equations cannot predict the time lag in the radial directions. It was previously noted that the unsteady conical Euler equations assume instantaneous propagation of disturbances in the radial directions. However, as the free-stream Mach number increases and the reduced frequency of oscillation decreases, this approximation improves. Although the cases presented in this work are not for extremely high Mach numbers, the reduced frequency of oscillation is low. For example, at a reduced frequency of 0.103, the phase shift from the apex to the trailing edge is approximately 7°. The effects of this phase lag cannot at this time be accurately quantified. However, if an analogy is made between the conical calculations and the computational work done on two-dimensional airfoils, then the conical results can be thought of in terms of crossflow sectional properties of the delta wing. These conical studies can then predict qualitative information about the sectional properties of the delta wing at different flow conditions, which can give insight and direction to subsequent three-dimensional calculations. Also, as in this study, the conical equations can act as an efficient test-bed for developing analysis methods that can be directly extended to three-dimensional calculations.

Active Roll-Suppression Results

An active rate-feedback control law was implemented in an attempt to suppress the wing-rock motion. To determine an appropriate value for the gain, a stability analysis was derived by again using the nondimensional rolling equation of motion given by

$$\phi'' = C_1 C_l \tag{25}$$

Assuming that the rolling-moment coefficient can be written as the superposition of the rolling-moment-coefficient transfer functions for ϕ and δ, then

$$C_l = C_{l_\phi}\phi + C_{l_\delta}\delta \tag{29}$$

Substituting the control law from equation (24) into equation (29) gives

$$C_l = C_{l_\phi}\phi + C_{l_\delta}K_v\phi' \tag{30}$$

Then, for simple harmonic motion,

$$\left.\begin{aligned} C_l = \{&[\mathrm{Re}(C_{l_\phi}) - kM_\infty K_v\ \mathrm{Im}(C_{l_\delta})] \\ &+ i[\mathrm{Im}(C_{l_\phi}) + kM_\infty K_v\ \mathrm{Re}(C_{l_\delta})]\} \end{aligned}\right\} \tag{31}$$

As before, the first term on the right-hand side of equation (31) represents an aerodynamic stiffness, and the second term represents an aerodynamic damping. Therefore, stabilizing the motion of the wing requires that the aerodynamic damping be positive, or that

$$\mathrm{Im}(C_{l_\phi}) + kM_\infty K_v\ \mathrm{Re}(C_{l_\delta}) < 0 \tag{32}$$

Solving for the gain yields

$$K_v > \frac{-1}{kM_\infty}\frac{\mathrm{Im}(C_{l_\phi})}{\mathrm{Re}(C_{l_\delta})} \tag{33}$$

A pulse analysis was performed to determine the rolling-moment-coefficient transfer function for δ at $\alpha = 30°$ (Pulse amplitude = 1°). The transfer function from this analysis (fig. 12) indicates that for values of reduced frequency less than 0.5, the real part of C_{l_δ} is negative. Considering equation (33) and recalling from figure 6(c) that the values of $\mathrm{Im}(C_{l_\phi})$ for $k < 0.5$ are positive, the value of K_v must be positive to suppress wing rock. The value of K_v actually needs to be greater than that determined by evaluating the right-hand side of equation (33) to stabilize the wing, since the preceding analysis assumes simple harmonic motion. For the flow conditions considered herein, the value for the gain that produces a neutrally stable (or simple harmonic) response is $K_v = 0.35$. The free-to-roll analysis with active rate-feedback control was performed for $K_v = 0.25$, 0.40, and 0.50. The time histories of the wing motion are shown in figure 13. As expected, the time history for $K_v = 0.50$ (fig. 13(a)) indicates a damped response. Similarly, the response for $K_v = 0.40$ (fig. 13(b)) is also damped, although at a smaller rate than for $K_v = 0.50$. The response of the wing for $K_v = 0.25$ (fig. 13(c)) indicates that the response is no longer damped. However, a comparison with the results of figure 10(c) ($K_v = 0$) shows that the active rate-feedback control reduces the growth rate of the response. The maximum flap deflection commanded by the control law during these free-response calculations was in the range of 1° to 2°.

Concluding Remarks

A conical Euler analysis method was developed to study unsteady, vortex-dominated flows about rolling, highly swept delta wings undergoing either forced motions or free-to-roll motions that include active roll suppression. The flow solver of the code involves a multistage, Runge-Kutta time-stepping scheme that uses a cell-centered, finite-volume, spatial discretization of the Euler equations on an unstructured grid of triangles. The code allows for the additional analysis of the free-to-roll case by simultaneously integrating in time the rigid-body equation of motion with the governing flow equations. Results are presented for a delta wing with a 75° swept, sharp leading edge at a free-stream Mach number of 1.2 and at 10°, 20°, and 30° angle of attack α. At the lower angles of attack (10° and 20°), forced-harmonic analyses indicate that the rolling-moment coefficients provide a positive damping, which is verified by free-to-roll calculations. In contrast, at the higher angle of attack (30°), a forced-harmonic analysis indicates that the rolling-moment coefficient provides negative damping at the small roll amplitudes. A free-to-roll calculation for this case produces an initially divergent response, but as the amplitude of motion grows with time, the response transitions to a wing-rock type of limit cycle oscillation, which is characteristic of highly swept delta wings. The wing-rock motion was subsequently suppressed, however, by the use of an active rate-feedback control law and antisymmetrically deflected leading-edge flaps. The methodology developed is directly extendable to three-dimensional calculations.

Acknowledgments

The authors would like to acknowledge Ken Morgan of the University College of Swansea, Swansea, U.K., and Jaime Peraire of the Imperial College of Science, Technology and Medicine, London, England, for providing the advancing-front method, grid-generation program that was used to generate the grid in the present study. The authors would also like to acknowledge Robert W. Neely of Lockheed Engineering & Sciences Company, Hampton, Virginia, for his assistance in the generation of color graphic figures.

NASA Langley Research Center
Hampton, VA 23681-0001
December 15, 1992

References

1. *High Angle-of-Attack Aerodynamics.* AGARD-LS-121, Dec. 1982.

2. Campbell, James F.; Osborn, Russell F.; and Foughner, Jerome T., Jr., eds.: *Vortex Flow Aerodynamics,* Volume I. NASA CP-2416, 1986.

3. *Manoeuvre Limitations of Combat Aircraft.* AGARD-AR-155A, Aug. 1979.

4. Hummel, -Ing. Dietrich: Documentation of Separated Flows for Computational Fluid Dynamics Validation. *Validation of Computational Fluid Dynamics,* Volume 2: Poster Papers, AGARD-CP-437, Vol. 2, Dec. 1988, pp. P15-1–P15-24.

5. Kjelgaard, Scott O.; and Sellers, William L., III: Detailed Flowfield Measurements Over a 75° Swept Delta Wing for Code Validation. Paper presented at the AGARD Symposium on Validation of Computational Fluid Dynamics (Lisbon, Portugal), May 2–5, 1988.

6. Squire, L. C.: Leading-Edge Separations and Cross-Flow Shocks on Delta Wings. *AIAA J.,* vol. 23, no. 3, Mar. 1985, pp. 321–325.

7. Miller, David S.; and Wood, Richard M.: *Lee-Side Flow Over Delta Wings at Supersonic Speeds.* NASA TP-2430, 1985.

8. Nguyen, Luat T.; Yip, Long P.; and Chambers, Joseph R.: Self-Induced Wing Rock of Slender Delta Wings. AIAA-81-1883, Aug. 1981.

9. Levin, Daniel; and Katz, Joseph: Dynamic Load Measurements With Delta Wings Undergoing Self-Induced Roll Oscillations. *J. Aircr.,* vol. 21, no. 1, Jan. 1984, pp. 30–36.

10. Jun, Young-Whoon; and Nelson, Robert C.: Leading-Edge Vortex Dynamics on a Slender Oscillating Wing. *J. Aircr.,* vol. 25, no. 9, Sept. 1988, pp. 815–819.

11. Arena, A. S., Jr.; and Nelson, R. C.: The Effect of Asymmetric Vortex Wake Characteristics on a Slender Delta Wing Undergoing Wing Rock Motion. *A Collection of Technical Papers—AIAA Atmospheric Flight Mechanics Conference,* Aug. 1989, pp. 16–24. (Available as AIAA-89-3348-CP.)

12. Ng, T. Terry: Flow Visualization Study of Delta Wings in Wing-Rock Motion. *A Collection of Technical Papers—AIAA 7th Applied Aerodynamics Conference,* July–Aug. 1989, pp. 194–204. (Available as AIAA-89-2187-CP.)

13. Hoeijmakers, H. W. M.: Computational Vortex Flow Aerodynamics. *Aerodynamics of Vortical Type Flows in Three Dimensions,* AGARD-CP-342, July 1983, pp. 18-1–18-35.

14. Newsome, Richard W.; and Kandil, Osama A.: Vortical Flow Aerodynamics—Physical Aspects and Numerical Simulation. AIAA-87-0205, Jan. 1987.

15. Hsu, Chung-Hao; and Lan, C. Edward: Theory of Wing Rock. *J. Aircr.,* vol. 22, no. 10, Oct. 1985, pp. 920–924.

16. Konstadinopoulos, P.; Mook, D. T.; and Nayfeh, A. H.: Subsonic Wing Rock of Slender Delta Wings. *J. Aircr.,* vol. 22, no. 3, Mar. 1985, pp. 223–228.

17. Elzebda, J. M.; Nayfeh, A. H.; and Mook, D. T.: Development of an Analytical Model of Wing Rock for Slender Delta Wings. *J. Aircr.,* vol. 26, no. 8, Aug. 1989, pp. 737–743.

18. Nayfeh, A. H.; Elzebda, J. M.; and Mook, D. T.: Analytical Study of the Subsonic Wing-Rock Phenomenon for Slender Delta Wings. *J. Aircr.,* vol. 26, no. 9, Sept. 1989, pp. 805–809.

19. Newsome, Richard W.; and Thomas, James L.: Computation of Leading-Edge Vortex Flows. *Vortex Flow Aerodynamics,* Volume I, James F. Campbell, Russell F. Osborn, and Jerome T. Foughner, Jr., eds., NASA CP-2416, 1986, pp. 305–330.

20. Kandil, Osama A.; and Chuang, Andrew: Influence of Numerical Dissipation in Computing Supersonic Vortex-Dominated Flows. Influence of Numerical Dissipation in Computing Supersonic Vortex-Dominated Flows. AIAA-86-1073, May 1986.

21. Chakravarthy, Sukumar R.; and Ota, Dale K.: Numerical Issues in Computing Inviscid Supersonic Flow Over Conical Delta Wings. AIAA-86-0440, Jan. 1986.

22. Murman, Earll M.; Powell, Kenneth G.; Miller, David S.; and Wood, Richard M.: Comparison of Computations and Experimental Data for Leading Edge Vortices—Effects of Yaw and Vortex Flaps. AIAA-86-0439, Jan. 1986.

23. Murman, Earll M.; and Rizzi, Arthur: Applications of Euler Equations to Sharp Edge Delta Wings With Leading Edge Vortices. *Applications of Computational Fluid Dynamics in Aeronautics,* AGARD-CP-412, Nov. 1986, pp. 15-1–15-13.

24. McMillin, S. N.; Thomas, J. L.; and Murman, E. M.: Euler and Navier-Stokes Solutions for the Leeside Flow Over Delta Wings at Supersonic Speeds. *A Collection of Technical Papers—AIAA 5th Applied Aerodynamics Conference,* Aug. 1987, pp. 14–33. (Available as AIAA-87-2270.)

25. Fujii, Kozo: A Method To Increase the Accuracy of Vortical Flow Simulations. *A Collection of Technical Papers—AIAA 6th Applied Aerodynamics Conference,* June 1988, pp. 321–328. (Available as AIAA-88-2562-CP.)

26. Powell, Kenneth G.; Murman, Earll M.; Perez, Eric S.; and Baron, Judson R.: Total Pressure Loss in Vortical Solutions of the Conical Euler Equations. *AIAA J.,* vol. 25, no. 3, Mar. 1987, pp. 360–368.

27. Kandil, Osama A.; and Chuang, Andrew H.: Computation of Steady and Unsteady Vortex Dominated Flows. AIAA-87-1462, June 1987.

28. Kandil, Osama A.; and Chuang, Andrew H.: Unsteady Navier-Stokes Computations Past Oscillating Delta Wing at High Incidence. AIAA-89-0081, Jan. 1989.

29. Batina, John T.: Vortex-Dominated Conical-Flow Computations Using Unstructured Adaptively-Refined Meshes. AIAA-89-1816, June 1989.

30. Lee, Elizabeth M.; and Batina, John T.: *Conical Euler Solution for a Highly-Swept Delta Wing Undergoing Wing-Rock Motion.* NASA TM-102609, 1990.

31. Lee, Elizabeth M.; and Batina, John T.: Conical Euler Simulation and Active Suppression of Delta Wing Rocking Motion. *High-Angle-of-Attack Technology,* Volume I, Joseph R. Chambers, William P. Gilbert, and Luat T. Nguyen, eds., NASA CP-3149, Part 3, 1992, pp. 1149–1170.

32. Lee, Elizabeth M.; and Batina, John T.: Conical Euler Methodology for Unsteady Vortical Flows About Rolling Delta Wings. AIAA-91-0730, Jan. 1991.

33. Kandil, Osama A.; and Salman, Ahmed A.: Effects of Leading-Edge Flap Oscillation on Unsteady Delta Wing Flow and Rock Control. AIAA-91-1796, June 1991.

34. Karagounis, T.; Maxworthy, T.; and Spedding, G. R.: Generation and Control of Separated Vortices Over a Delta Wing by Means of Leading Edge Flaps. AIAA-89-0997, Mar. 1989.

35. Ellis, D. G.; and Stollery, J. L.: The Behaviour and Performance of Leading-Edge Vortex Flaps. *ICAS Proceedings 1988—16th Congress of the International Council of*

the Aeronautical Sciences, Aug.–Sept. 1988, pp. 758–765. (Available as ICAS-88-4.5.2.)

36. Ng, T. T.: On Leading Edge Vortex and Its Control. *A Collection of Technical Papers—AIAA Atmospheric Flight Mechanics Conference,* Aug. 1989, pp. 1–15. (Available as AIAA-89-3346-CP.)

37. Wood, N. J.; Roberts, L.; and Celik, Z.: The Control of Asymmetric Vortical Flows Over Delta Wings at High Angles of Attack. *A Collection of Technical Papers—AIAA Atmospheric Flight Mechanics Conference,* Aug. 1989, pp. 484–491. (Available as AIAA-89-3347-CP.)

38. Jameson, A.; and Mavriplis, D.: Finite Volume Solution of the Two-Dimensional Euler Equations on a Regular Triangular Mesh. *AIAA J.,* vol. 24, no. 4, Apr. 1986, pp. 611–618.

39. Mavriplis, D. J.: Multigrid Solution of the Two-Dimensional Euler Equations on Unstructured Triangular Meshes. *AIAA J.,* vol. 26, no. 7, July 1988, pp. 824–831.

40. Jameson, A.; Schmidt, Wolfgang; and Turkel, Eli: Numerical Solution of the Euler Equations by Finite Volume Methods Using Runge Kutta Time Stepping Schemes. AIAA-81-1259, June 1981.

41. Venkatakrishnan, V.: Computation of Unsteady Transonic Flows Over Moving Airfoils. Ph.D. Thesis, Princeton Univ., 1987.

42. Batina, John T.: Unsteady Euler Airfoil Solutions Using Unstructured Dynamic Meshes. AIAA-89-0115, Jan. 1989.

43. Seidel, David A.; Bennett, Robert M.; and Whitlow, Woodrow, Jr.: An Exploratory Study of Finite-Difference Grids for Transonic Unsteady Aerodynamics. AIAA-83-0503, Jan. 1983.

44. Seidel, David A.; Bennett, Robert M.; and Ricketts, Rodney H.: Some Recent Applications of XTRAN3S. AIAA-83-1811, July 1983.

45. Morgan, K.; and Peraire, J.: Finite Element Methods for Compressible Flows. *Computational Fluid Dynamics,* LS-1987-04, Von Karman Inst. for Fluid Dynamics, Mar. 1987.

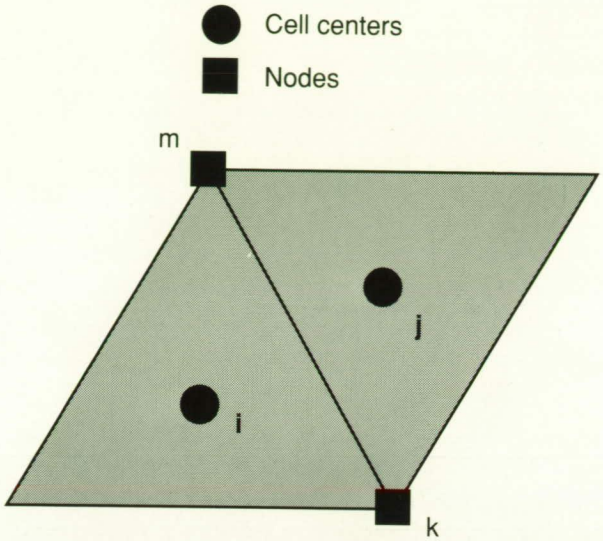

Figure 1. Example of a central-difference type of differencing approach.

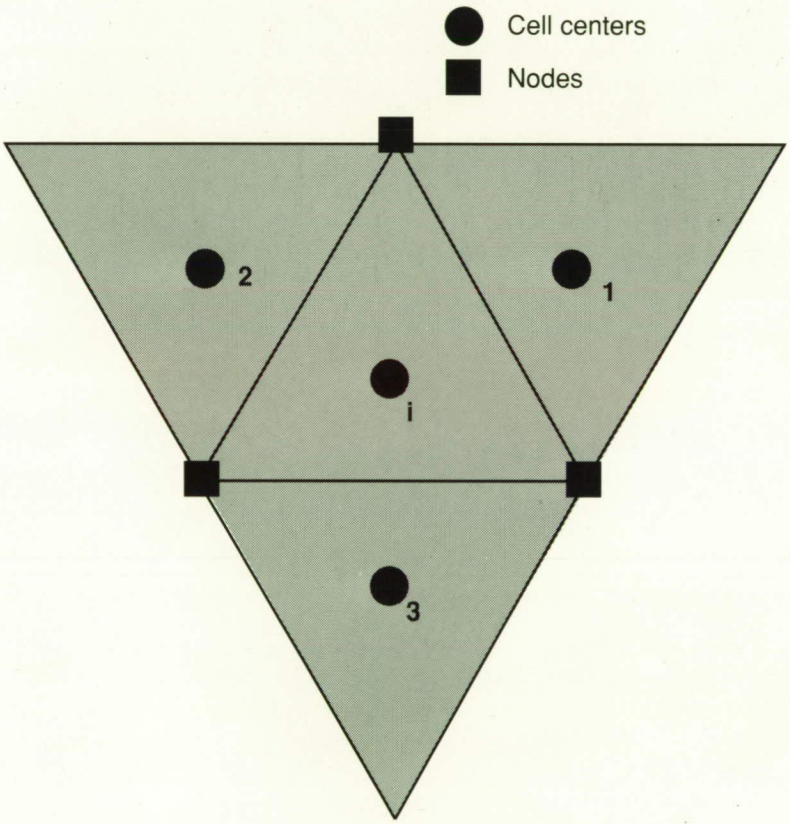

Figure 2. Difference stencil for harmonic operator.

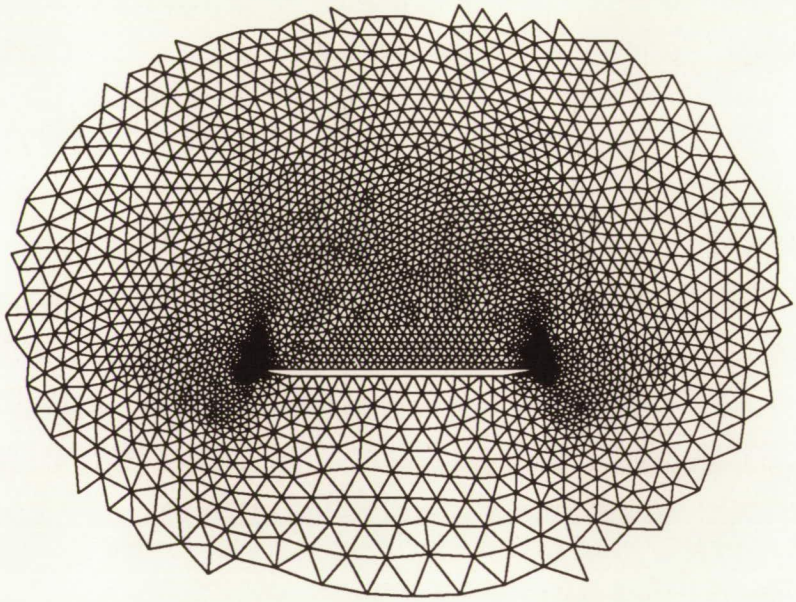

Figure 3. Partial view of unstructured grid about 75° swept delta wing.

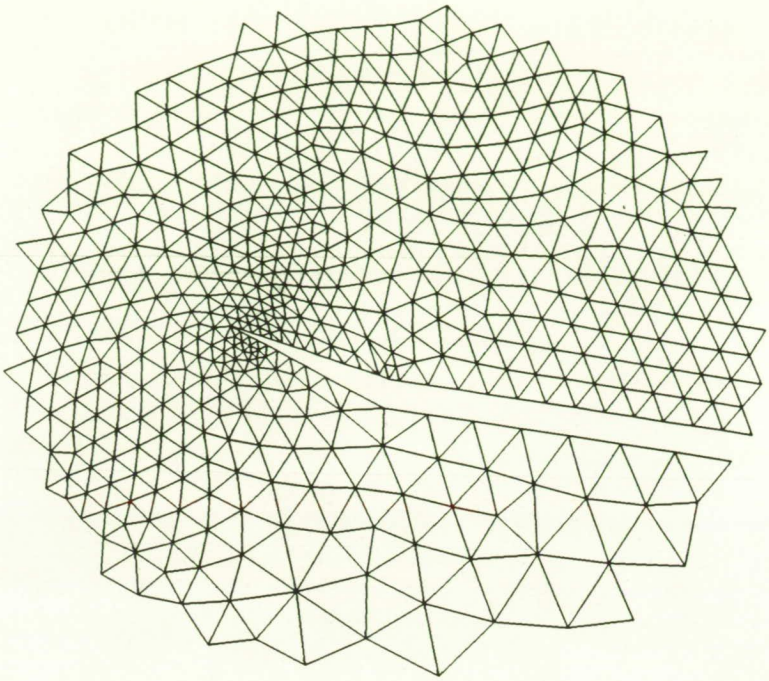

(a) $\delta = 10°$.

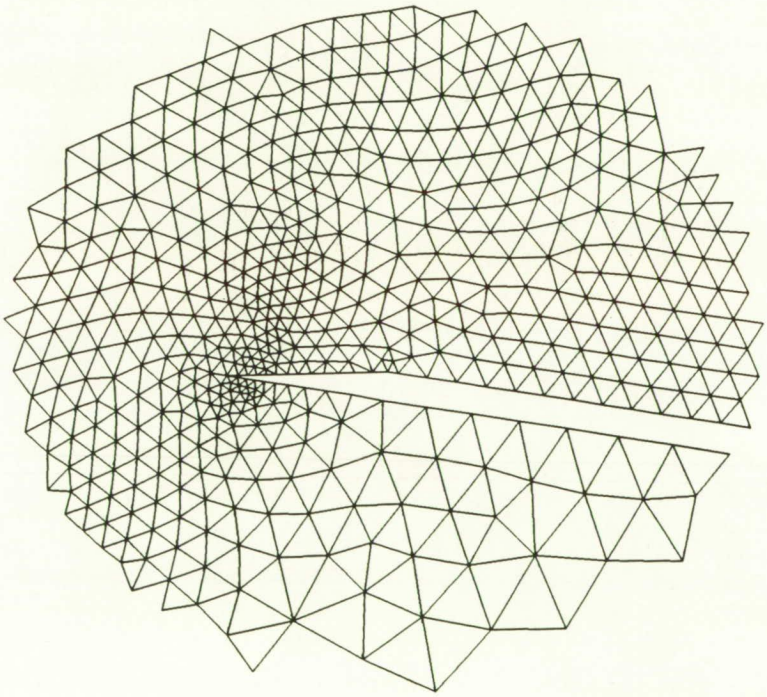

(b) $\delta = -10°$.

Figure 4. Partial view of deforming mesh about deflected leading-edge flap.

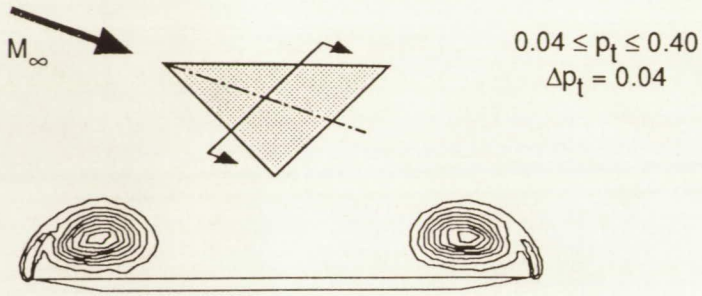

(a) $\alpha = 10°$.

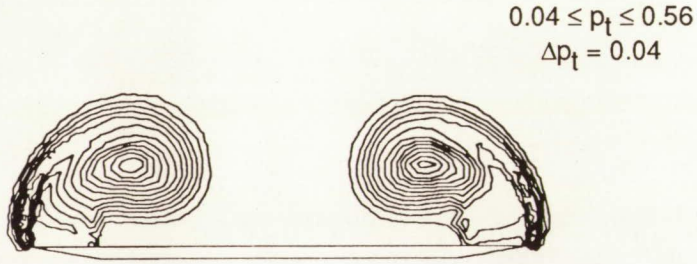

(b) $\alpha = 20°$.

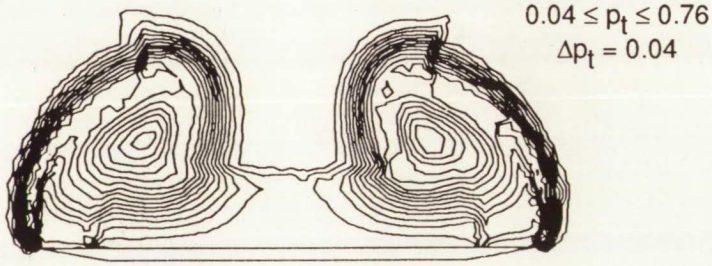

(c) $\alpha = 30°$.

Figure 5. Effects of angle of attack on steady-state total-pressure-loss contours for a 75° swept delta wing at $M_\infty = 1.2$.

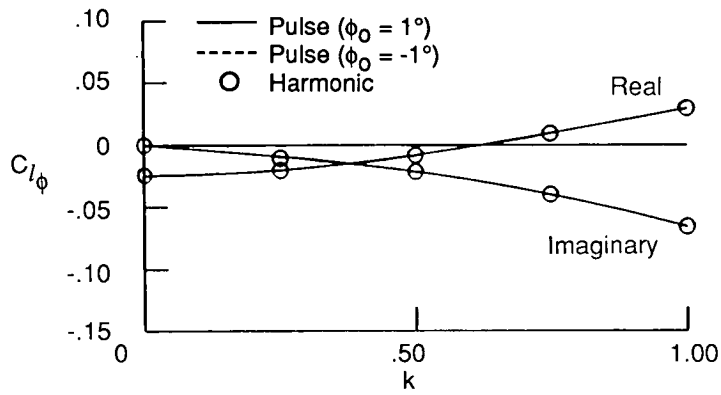

(a) $\alpha = 10°$.

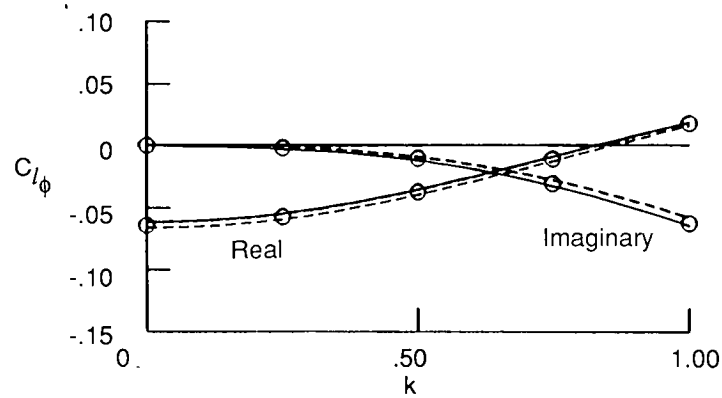

(b) $\alpha = 20°$.

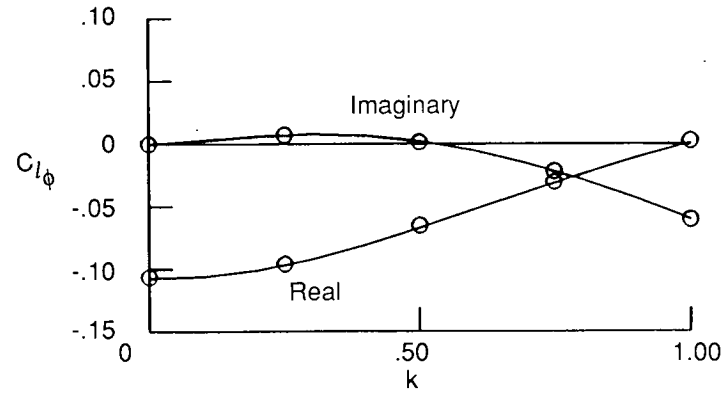

(c) $\alpha = 30°$.

Figure 6. Effects of angle of attack on rolling-moment-coefficient transfer function versus reduced frequency for a 75° swept delta wing at $M_\infty = 1.2$.

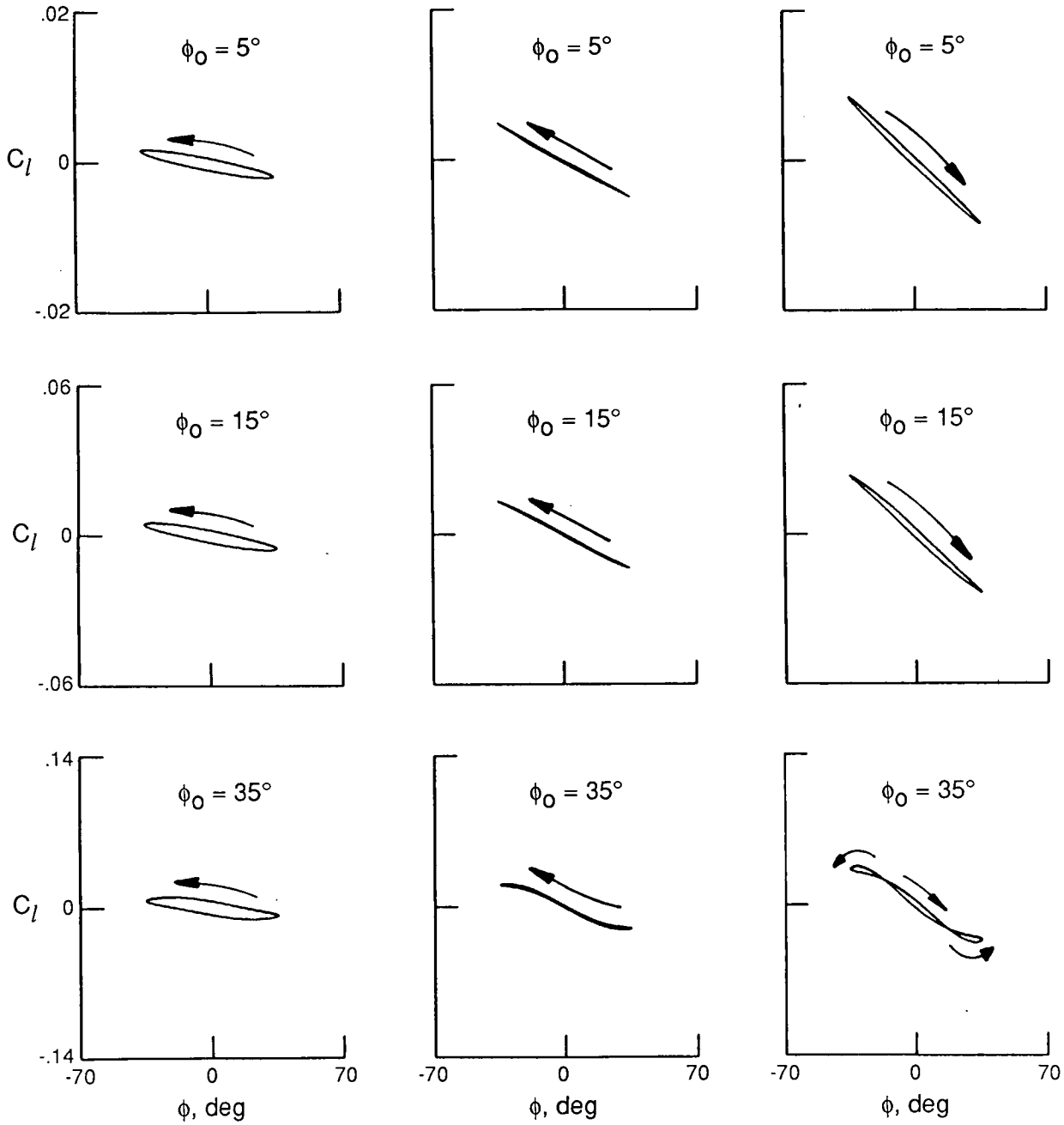

(a) $\alpha = 10°$. (b) $\alpha = 20°$. (c) $\alpha = 30°$.

Figure 7. Effects of angle of attack on rolling-moment coefficient versus instantaneous roll angle for a 75° swept delta wing at $M_\infty = 1.2$ and $k = 0.25$.

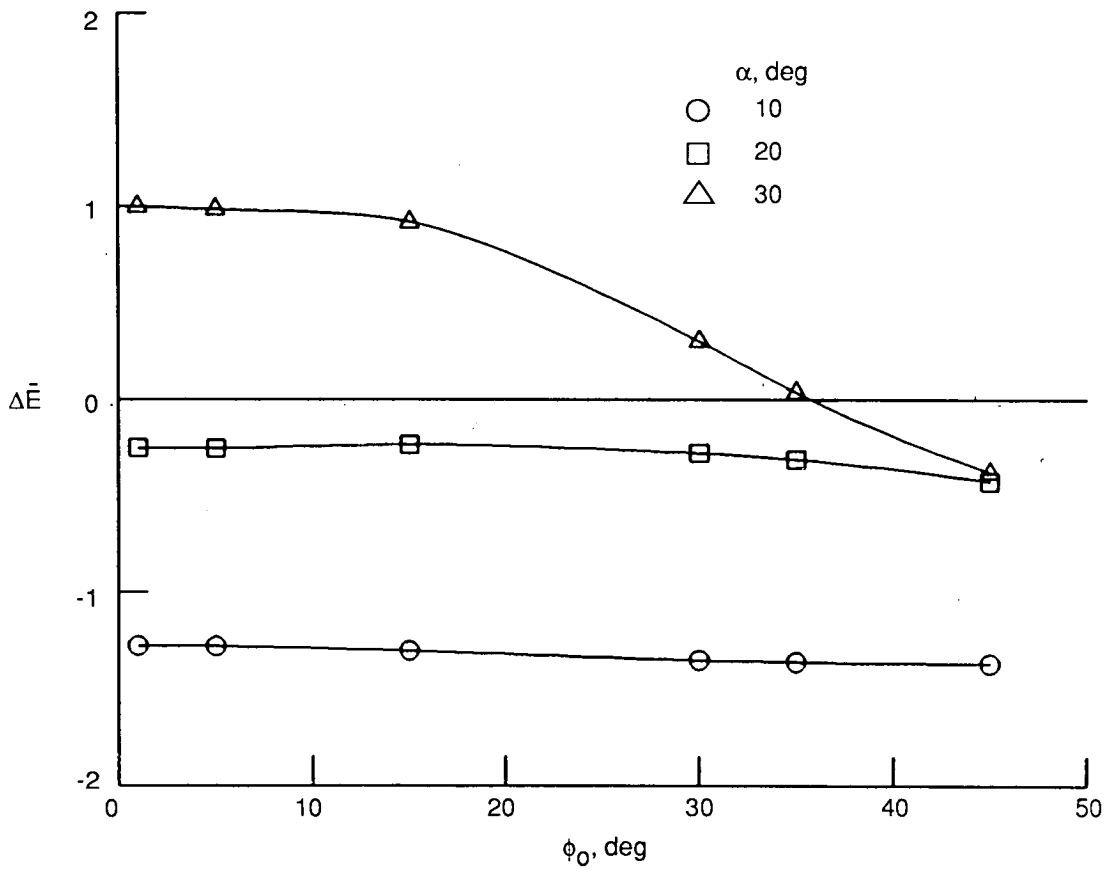

Figure 8. Effects of angle of attack and roll amplitude on normalized energy exchange versus roll amplitude for a 75° swept delta wing at $M_\infty = 1.2$ and $k = 0.25$.

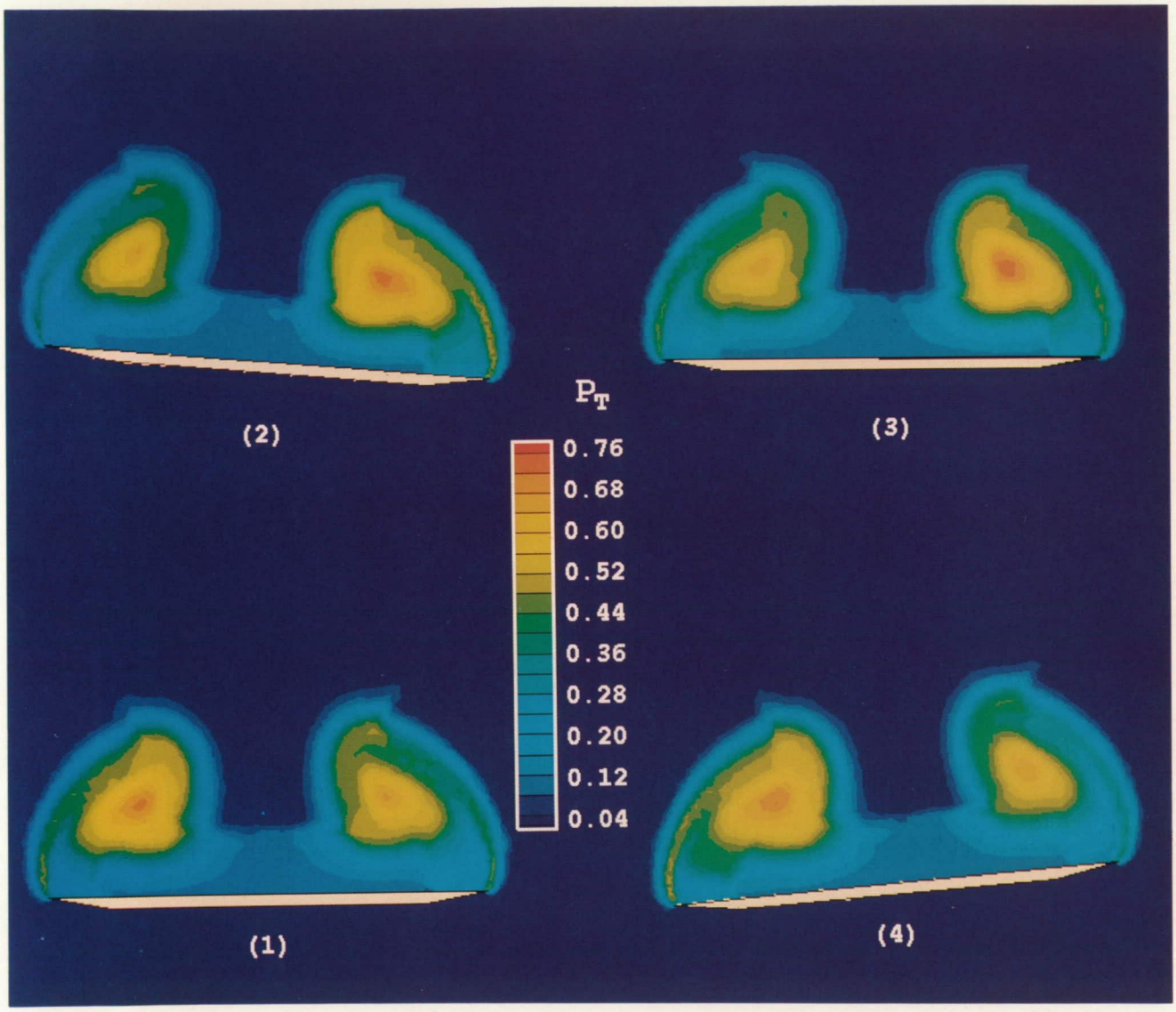

(a) $\phi_o = 5°$.

Figure 9. Total-pressure-loss contours during a cycle of harmonic rolling motion for a 75° swept delta wing at $M_\infty = 1.2$, $\alpha = 30°$, and $k = 0.25$.

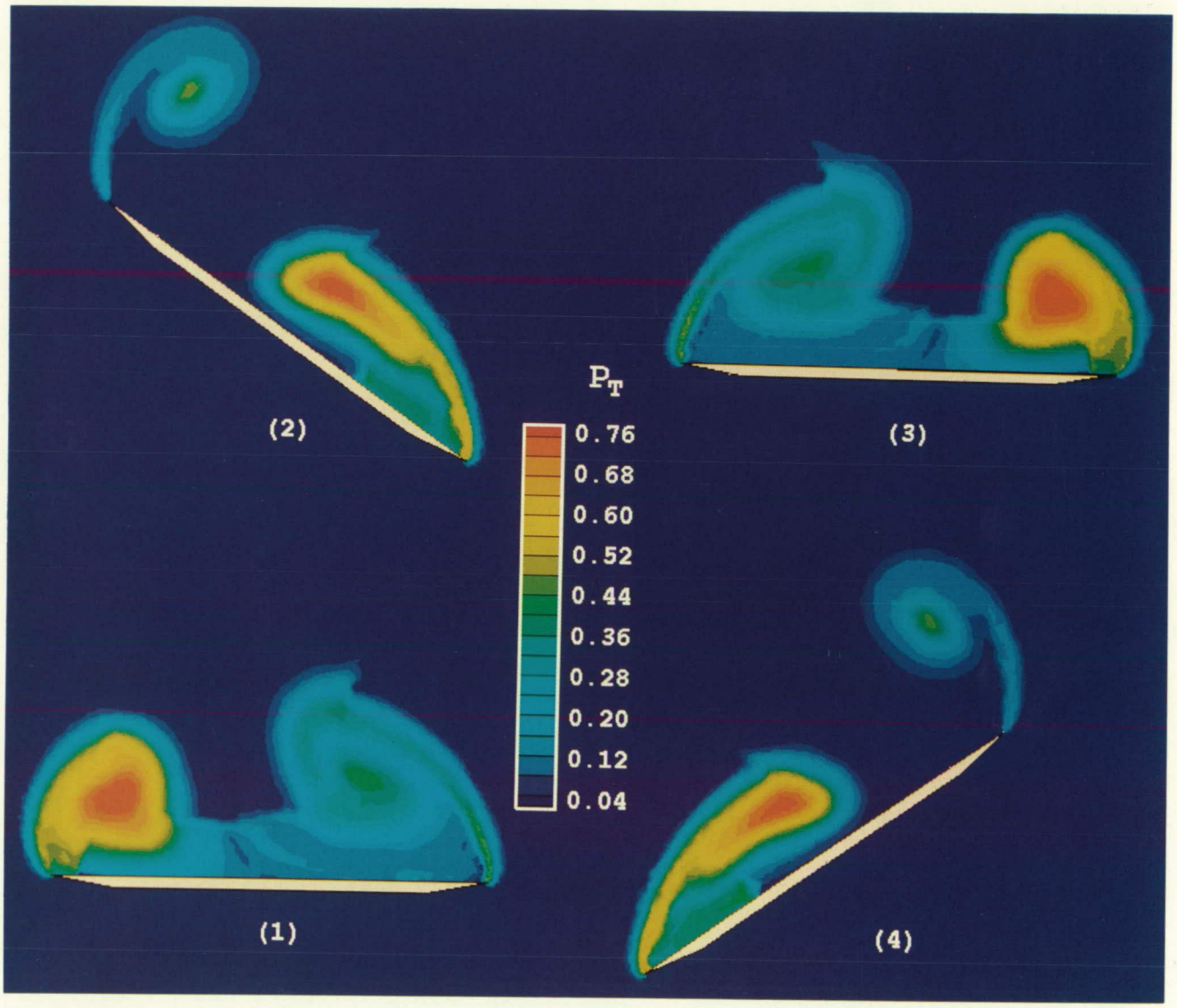

(b) $\phi_o = 35°$.

Figure 9. Concluded.

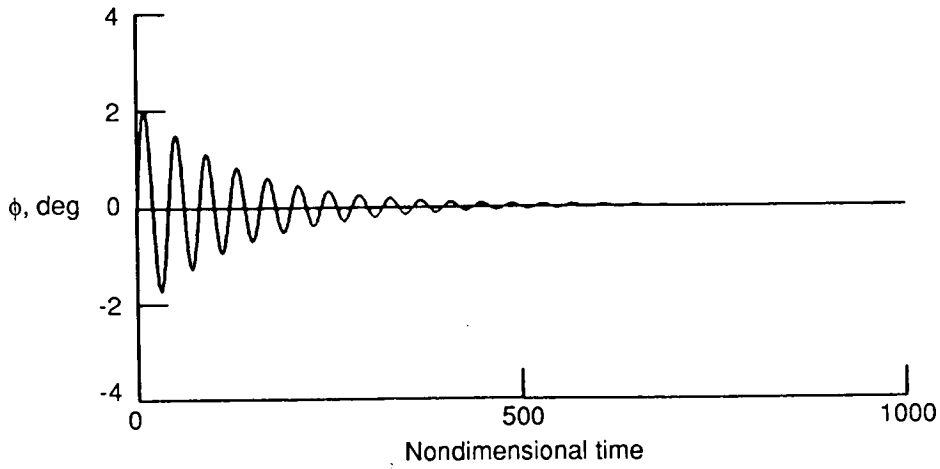

(a) $\alpha = 10°$.

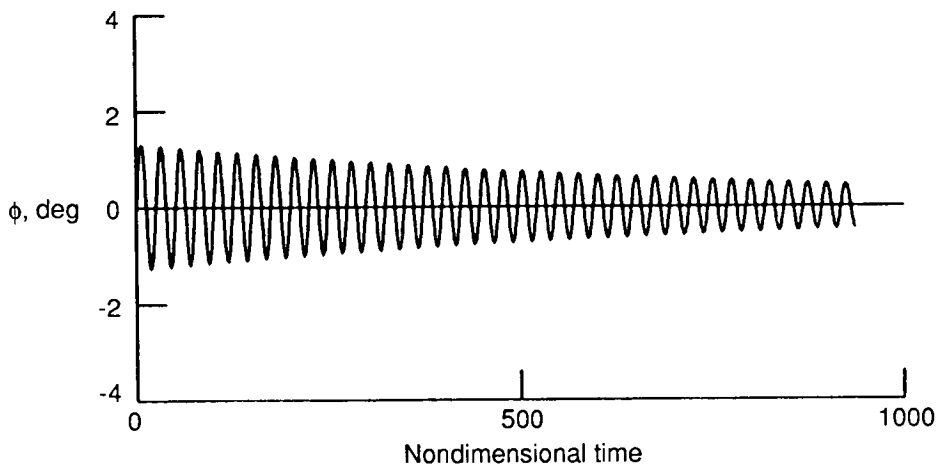

(b) $\alpha = 20°$.

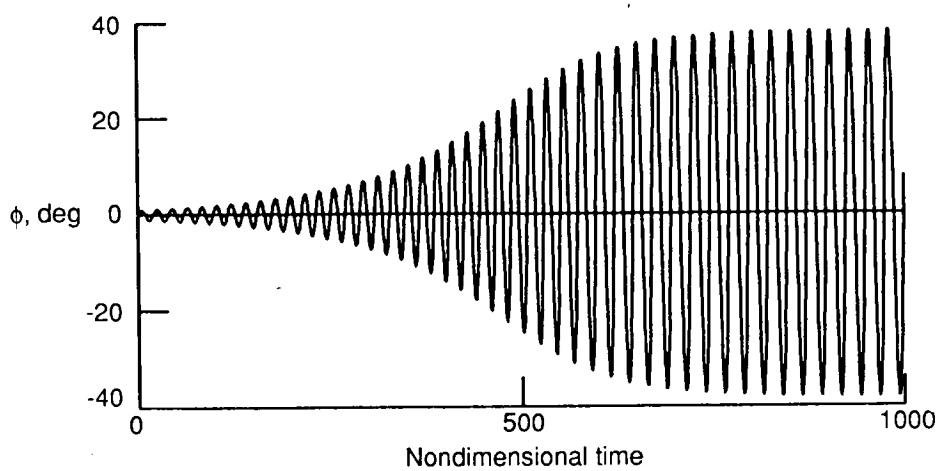

(c) $\alpha = 30°$.

Figure 10. Effects of angle of attack on free-to-roll response for a 75° swept delta wing at $M_\infty = 1.2$.

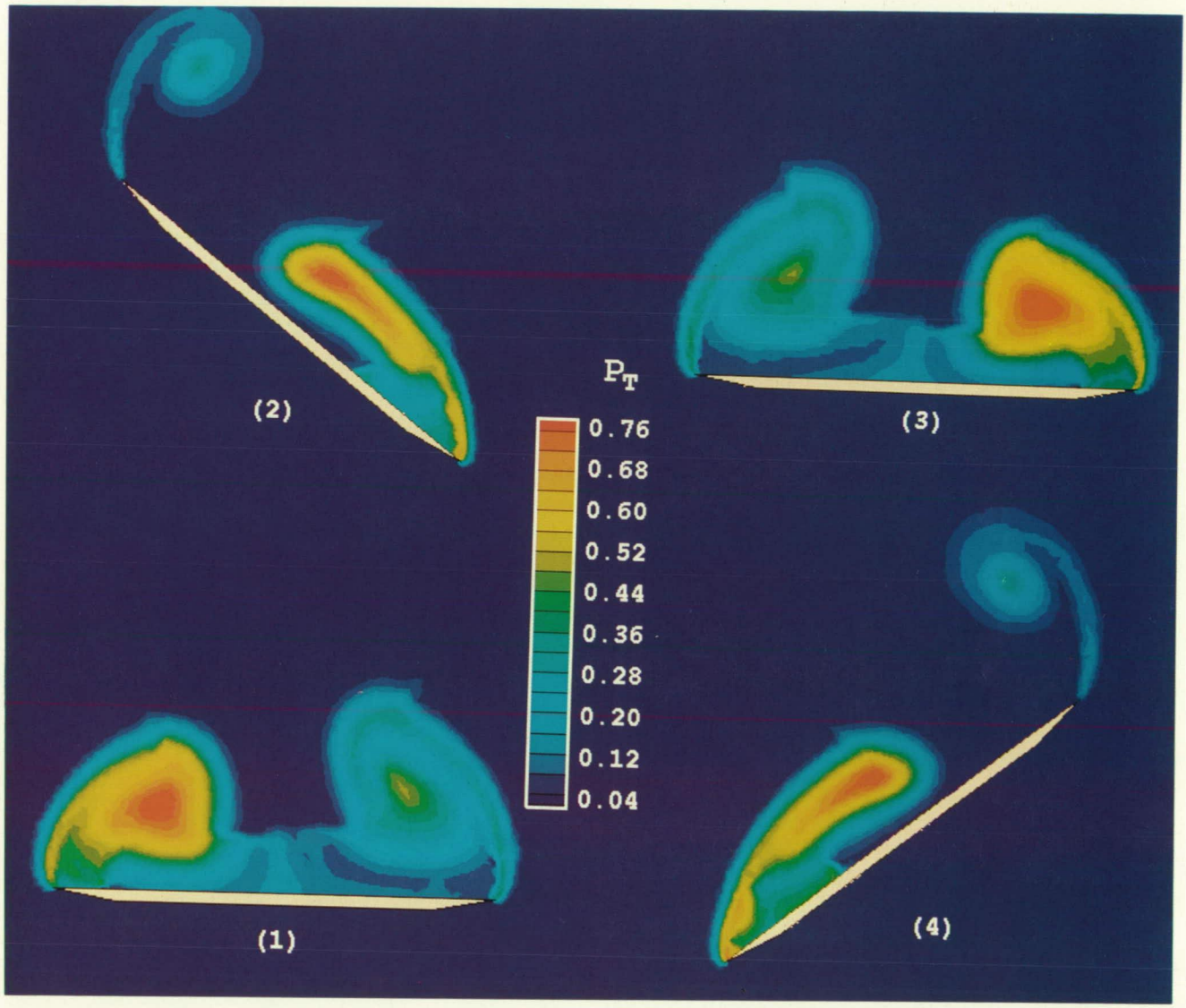

Figure 11. Total-pressure-loss contours during a cycle of wing rock for a 75° swept delta wing at $M_\infty = 1.2$ and $\alpha = 30°$.

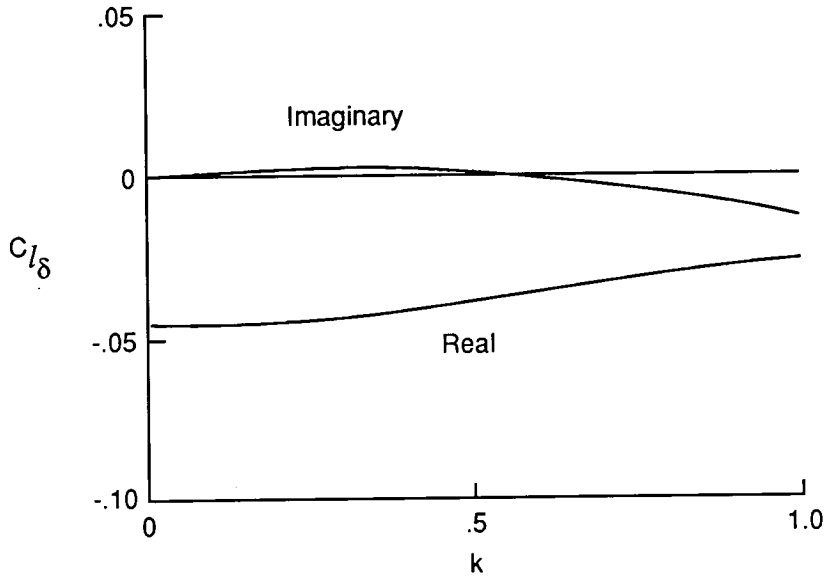

Figure 12. Rolling-moment-coefficient transfer function for flap versus reduced frequency for a 75° swept delta wing at $M_\infty = 1.2$. Pulse amplitude = 1°.

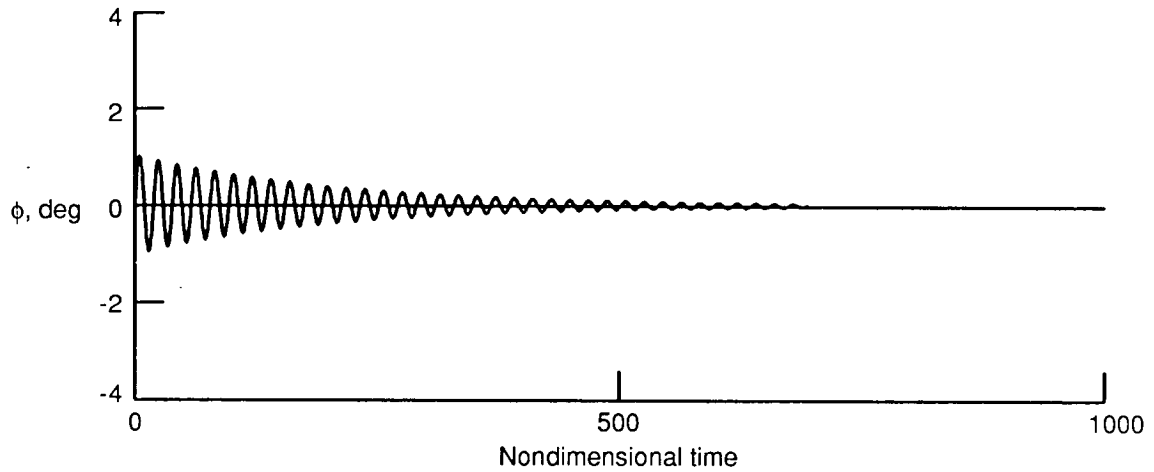

(a) $K_v = 0.50$.

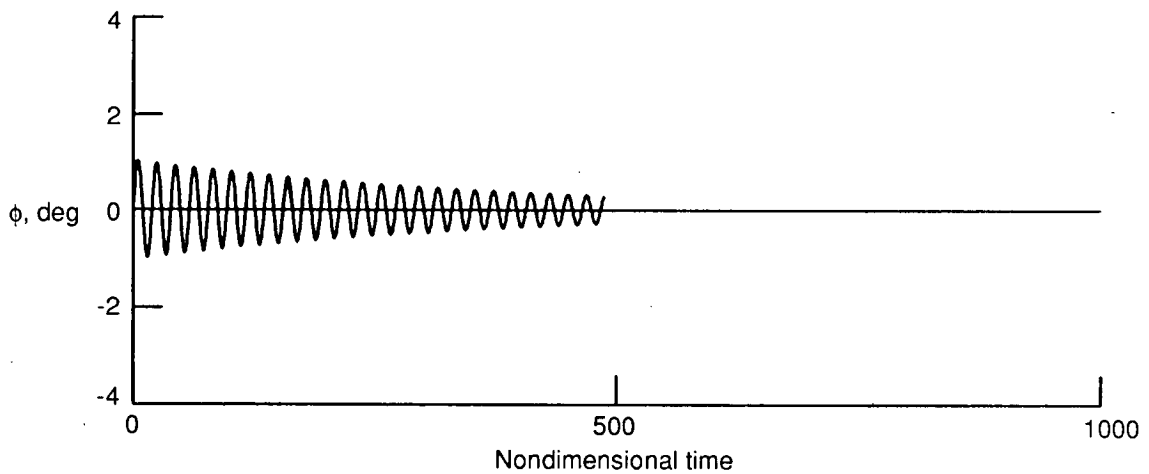

(b) $K_v = 0.40$.

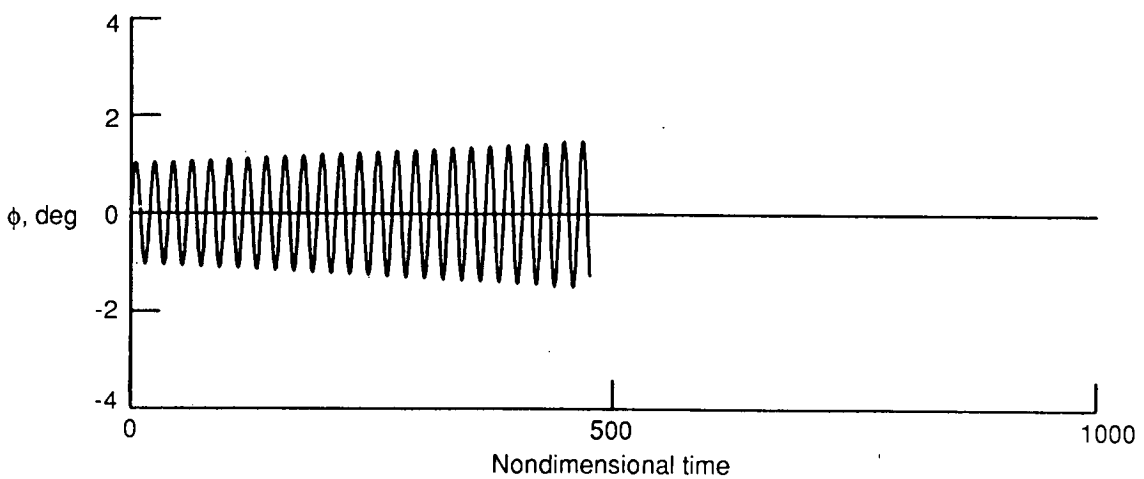

(c) $K_v = 0.25$.

Figure 13. Free-to-roll response with active rate-feedback control for a 75° swept delta wing at $M_\infty = 1.2$ and $\alpha = 30°$.

REPORT DOCUMENTATION PAGE

Form Approved
OMB No. 0704-0188

Public reporting burden for this collection of information is estimated to average 1 hour per response, including the time for reviewing instructions, searching existing data sources, gathering and maintaining the data needed, and completing and reviewing the collection of information. Send comments regarding this burden estimate or any other aspect of this collection of information, including suggestions for reducing this burden, to Washington Headquarters Services, Directorate for Information Operations and Reports, 1215 Jefferson Davis Highway, Suite 1204, Arlington, VA 22202-4302, and to the Office of Management and Budget, Paperwork Reduction Project (0704-0188), Washington, DC 20503.

1. AGENCY USE ONLY *(Leave blank)*

2. REPORT DATE
March 1993

3. REPORT TYPE AND DATES COVERED
Technical Paper

4. TITLE AND SUBTITLE
Conical Euler Analysis and Active Roll Suppression for Unsteady Vortical Flows About Rolling Delta Wings

5. FUNDING NUMBERS
WU 505-63-50-12

6. AUTHOR(S)
Elizabeth M. Lee-Rausch and John T. Batina

7. PERFORMING ORGANIZATION NAME(S) AND ADDRESS(ES)
NASA Langley Research Center
Hampton, VA 23681-0001

8. PERFORMING ORGANIZATION REPORT NUMBER
L-17059

9. SPONSORING/MONITORING AGENCY NAME(S) AND ADDRESS(ES)
National Aeronautics and Space Administration
Washington, DC 20546-0001

10. SPONSORING/MONITORING AGENCY REPORT NUMBER
NASA TP-3259

11. SUPPLEMENTARY NOTES

12a. DISTRIBUTION/AVAILABILITY STATEMENT
Unclassified–Unlimited

Subject Category 02

12b. DISTRIBUTION CODE

13. ABSTRACT *(Maximum 200 words)*
A conical Euler code was developed to study unsteady vortex-dominated flows about rolling, highly swept delta wings undergoing either forced motions or free-to-roll motions that include active roll suppression. The flow solver of the code involves a multistage, Runge-Kutta time-stepping scheme that uses a cell-centered, finite-volume, spatial discretization of the Euler equations on an unstructured grid of triangles. The code allows for the additional analysis of the free-to-roll case by simultaneously integrating in time the rigid-body equation of motion with the governing flow equations. Results are presented for a delta wing with a 75° swept, sharp leading edge at a free-stream Mach number of 1.2 and at 10°, 20°, and 30° angle of attack α. At the lower angles of attack (10° and 20°), forced-harmonic analyses indicate that the rolling-moment coefficients provide a positive damping, which is verified by free-to-roll calculations. In contrast, at the higher angle of attack (30°), a forced-harmonic analysis indicates that the rolling-moment coefficient provides negative damping at the small roll amplitudes. A free-to-roll calculation for this case produces an initially divergent response, but as the amplitude of motion grows with time, the response transitions to a wing-rock type of limit cycle oscillation, which is characteristic of highly swept delta wings. This limit cycle oscillation may be actively suppressed through the use of a rate-feedback control law and antisymmetrically deflected leading-edge flaps. Descriptions of the conical Euler flow solver and the free-to-roll analysis are included in this report. Results are presented that demonstrate how the systematic analysis of the forced response of the delta wing can be used to predict the stable, neutrally stable, and unstable free response of the delta wing. These results also give insight into the flow physics associated with unsteady vortical flows about delta wings undergoing forced motions and free-to-roll motions, including the active suppression of the wing-rock type phenomenon. The conical Euler methodology developed is directly extendable to three-dimensional calculations.

14. SUBJECT TERMS
Computational fluid dynamics; Unsteady aerodynamics; Vortical flow; Active control; Wing rock

15. NUMBER OF PAGES
28

16. PRICE CODE
A03

17. SECURITY CLASSIFICATION OF REPORT
Unclassified

18. SECURITY CLASSIFICATION OF THIS PAGE
Unclassified

19. SECURITY CLASSIFICATION OF ABSTRACT

20. LIMITATION OF ABSTRACT